Synthesis, Solution Structure and Phyla-selectivity of a Spider δ-Toxin That Slows Inactivation of Specific Voltage-gated Sodium Channel Subtypes*

Nahoko Yamaji[‡1], Michelle J. Little[§1], Hideki Nishio[¶], Bert Billen[‖], Elba Villegas[**], Yuji Nishiuchi[¶], Jan Tytgat[‖], Graham M. Nicholson[§2], and Gerardo Corzo[#3]

From the [‡]Suntory Institute for Bioorganic Research, Mishima-gun, Shimamoto-cho, Wakayamadai 1-1-1, Osaka 618-8503, Japan, the [§]Neurotoxin Research Group, Department of Medical & Molecular Biosciences, University of Technology, Sydney, Broadway, NSW 2007, Australia, the [¶]Peptide Institute Inc., Protein Research Foundation, Osaka, Japan, the [‖]Laboratory of Toxicology, University of Leuven, Campus Gasthuisberg, O&N2, PO Box 922, 3000 Leuven, Belgium, the [**]Centro de Investigacion en Biotecnologia UAEM, Av. Universidad 2001, Cuernavaca, Morelos 62210, Mexico, and the [#]Instituto de Biotecnologia-UNAM, Av. Universidad 2001, Cuernavaca, Morelos 62210, Mexico

[2] To whom correspondence should be addressed. Tel.: 61-2-9514-2230; Fax: 61-2-9514-8206; E-mail: Graham.Nicholson@uts.edu.au

[3] To whom correspondence should be addressed. Tel.: 52-777-329-1600; Fax: 52-777-317-2388; E-mail: corzo@ibt.unam.mx

Magi 4, now renamed δ-hexatoxin-Mg1a, is a 43-residue neurotoxic peptide from the venom of the hexathelid Japanese funnel-web spider (*Macrothele gigas*) with homology to δ-hexatoxins from Australian funnel-web spiders. It binds with high affinity to receptor site 3 on insect voltage-gated sodium (Na_V) channels but, unlike δ-hexatoxins, does not compete for the related site 3 in rat brain despite being previously shown to be lethal by intracranial injection. To elucidate differences in Na_V channel selectivity we have undertaken the first characterisation of a peptide toxin on a broad range of mammalian and insect Na_V channel subtypes showing that δ-hexatoxin-Mg1a selectively slows channel inactivation of mammalian $Na_V1.1$, $Na_V1.3$, and $Na_V1.6$ but more importantly shows higher affinity for insect Na_V1 (*para*) channels. Consequently, δ-hexatoxin-Mg1a induces tonic repetitive firing of nerve impulses in insect neurons accompanied by plateau potentials. In addition, we have chemically synthesised and folded δ-hexatoxin-Mg1a, ascertained the bonding pattern of the four disulfides and determined its three dimensional solution structure using NMR spectroscopy. Despite modest sequence homology, we show that key residues important for the activity of scorpion α-toxins and δ-hexatoxins are distributed in a topologically similar manner in δ-hexatoxin-Mg1a. However subtle differences in the toxin surfaces are important for the novel selectivity of δ-hexatoxin-Mg1a for certain mammalian and insect Na_V channel subtypes. As such, δ-hexatoxin-Mg1a provides us with a specific tool with which to study channel structure and function and determinants for phyla- and tissue-specific activity.

Voltage-gated sodium (Na_V)[4] channels are responsible for the generation and propagation of electrical signals in excitable cells. At least nine different genes encoding distinct Na_V channels isoforms have been identified, and functionally expressed, in mammals (1). They are characterized by their sensitivity to TTX, with $Na_V1.5$, $Na_V1.8$ and $Na_V1.9$ being TTX-insensitive or TTX-resistant and the remaining subtypes being sensitive to nanomolar concentrations of TTX. In addition, localization of the subtypes also varies, with $Na_V1.1$–1.3 mostly distributed in the central nervous system, $Na_V1.6$–1.9 principally located in the peripheral nervous system, and $Na_V1.4$ and $Na_V1.5$ found in skeletal and cardiac muscle, respectively. The structural diversity of Na_V channels also coincides with variations in physiological and pharmacological properties (2). In contrast, insects express only one gene (*para*) that undergoes extensive alternative splicing and RNA editing (3). The *para*-encoded Na_V channel is exceptionally well conserved across diverse orders of insects, with the level of identity ranging from 87 to 98% (3). This is one reason why insecticides that target insect Na_V channels have broad activity

across many insect orders. In contrast, *para*-type Na_V channels have significantly lower levels of identity with the various types of mammalian Na_V channels with the level of identity typically around 50–60% (3). This explains why a high degree of phylogenetic specificity can be achieved with both Na_V channel toxins and insecticides that target the Na_V channel.

At least seven distinct toxin binding sites have been identified by radioligand binding and electrophysiological studies on vertebrate and insect Na_V channels (4,5). Toxins interacting with these neurotoxin receptor site have been instrumental in the study of Na_V channel topology, function, and pharmacology (6). In particular, a wide range of scorpion *α*-toxins, sea anemone toxins and spider *δ*-hexatoxins [formerly *δ*-atracotoxins, (7)] compete for binding to receptor site-3 on the extracellular surface of Na_V channels. These polypeptide toxins all inhibit the fast inactivation of Na_V channels to prolong Na^+ currents (I_{Na}), despite huge diversity in primary and tertiary structures (8,9). Nevertheless, receptor site-3 has not yet been fully characterized but believed to involve domains DI/S5-S6, DIV/S5-S6 as well as DIV/S3-S4 (for references see (9). Most importantly, however, toxin characterization is often limited to studies using whole cell I_{Na} or binding studies on neuronal membranes where there are mixed populations of Na_V channel subtypes. For all of these toxins, the precise pattern of Na_V channel subtype selectivity is either unknown, or at best incomplete.

Recently, it was found that receptor site-3 was also recognized by a 43-residue spider toxin, originally named Magi 4, from the hexathelid spider *Macrothele gigas* (Iriomote, Japan). It binds with high affinity to insect Na_V channels but, similar to scorpion *α*-like toxins, does not compete for the related site-3 in rat brain synaptosomes, despite being lethal by intracranial injection (10). Magi 4 shares significant homology to four *δ*-hexatoxin (HXTX)-1 family peptides and *δ*-actinopoditoxin-Mb1a (formerly *δ*-missulenatoxin-Mb1a; Fig. 1) but no sequence homology to scorpion *α*-toxins. Neurochemical studies have shown that *δ*-HXTX-1 toxins compete at nanomolar concentrations with both anti-mammalian (e.g. Aah2, Lqh2) and anti-insect (e.g. Lqh*α*IT) scorpion toxins for site-3 (11-13). The three-dimensional structures of *δ*-HXTX-Ar1a and *δ*-HXTX-Hv1a peptides have been determined (14,15) and possess core *β* regions stabilized by four disulfide bonds, placing them in the inhibitory cystine knot (ICK) structural family (16).

The aim of this study was to firstly determine the solution structure of Magi 4 and secondly to investigate the ability of Magi 4 to discriminate between different Na_V channels subtypes. Here we report the tertiary structure of Magi 4 by ^{1}H-NMR and show its disulfide bonding pattern and 3D structure is homologous to *δ*-HXTX-1 toxins. We highlight the key residues in Magi 4 appear to be topologically similar to those residues known to be part of the pharmacophore for site-3 scorpion *α*-toxins, despite Magi 4 having a different overall structure to scorpion *α*-toxins (11). In addition, we provide a detailed characterization of the selectivity and mode of action of Magi 4 on nine cloned mammalian and insect Na_V channel subtypes, including a detailed characterization on insect neurotransmission. Given that the toxin potently slows the inactivation of Na_V channels it should be renamed *δ*-hexatoxin-Mg1a (*δ*-HXTX-Mg1a) in accordance with the rational nomenclature recently proposed for naming spider peptide toxins (7) (see ArachnoServer spider toxin database; http://www.arachnoserver.org).

EXPERIMENTAL PROCEDURES

Peptide synthesis– *δ*-HXTX-Mg1a (43 residues) was chemically synthesized by native chemical ligation involving the coupling of a Cys(17)1–19-thioester peptide (*N*-terminal 19 residues) and Cys20–43 peptide (*C*-terminal 24 residues). The *N*-terminal Cys residue of the former peptide was protected by the Acm group to prevent cyclization and oligomerization. The solid-phase synthesis of the Cys(17)1–19-thioester and Cys20–43 peptides were performed using a ABI 433A peptide synthesizer using the Boc strategy on a Boc-Asn(Xan)-S-CH_2-CH_2-CO-Leu-Pam resin (0.5 mmol) and Boc-Cys(4-MeBzl)-Merrifield resin (0.3 mmol), respectively. The peptide chains were elongated using *in situ* neutralization protocols of coupling with Boc-amino acid/HBTU/HOBt/DIEA (4/4/4/6 equiv.). After chain assembly was completed, the peptide resins obtained were treated with HF in the presence of *p*-cresol (to protect Trp residues) and 1,4-butanedithiol (as an oxygen scavenger) at –5 ºC for 1 h to remove all of the protecting and anchoring groups except the Acm group on the Cys[1] residue. The crude products were then purified by preparative RP-HPLC using a YMC-Pak ODS column (30 x 250 mm) to obtain 195 mg (16%) and 75 mg (8.4%) of purified peptides, respectively.

The *N*-terminal Cys(17)1-19-thioester and *C*-terminal Cys20-43 peptides were then allowed to ligate by solubilizing them in freshly degassed 0.1 M sodium phosphate buffer (10 ml), pH 8.4, containing 6 M guanidium hydrochloride (Gdn·HCl). Thiophenol (0.40 ml) was then added, the whole mixture stirred for 24 h at room temperature and then treated with DTT (1.6 mmol). After 20 min the pH was acidified to less than 2 using 1 M HCl. The mixture was washed with ether and Cys(17)1–43 peptide purified from the aqueous layers by preparative RP-HPLC using a linear gradient (20-40% CH_3CN in 0.1% TFA for 80 min) to obtain 51 mg (41%) of purified peptide.

To remove the Acm group, a 9.6 mM solution of Cys(17)1–43 (50 mg) was made up in 5 ml 95% TFA containing anisole (50 μl) and 0.77 mmol Ag trifluoroacetate was added and stirred for 2 h at room temperature. The product was precipitated as the Ag salt, by adding ether to the reaction mixture, and was dissolved in 0.1 M phosphate buffer, pH 8.4, containing 6 M Gdn·HCl. DTT (3.8 mmol) was added to the solution and stirred for 0.5 h at room temperature. After the addition of 1 M HCl, the resulting AgCl was removed by filtration and the filtrate was applied to preparative RP-HPLC using a linear gradient (20-40% CH_3CN in 0.1% TFA for 80 min) to obtain 23 mg (46% yield) of the reduced peptide (8 SH-peptide (1-43)).

The eight free cysteines were allowed to oxidize in air for 4 days at 4 °C in 0.1 M aqueous ammonium acetate (pH 7.6) containing 2 M Gdn·HCl, 0.1 mM GSSG and 1 mM GSH. The peptide:GSSG:GSH ratio was 1:10:100. The solution was then diluted 2-fold with cold water (4 °C) to a final peptide concentration of 5 μM. After 3 days at 4 °C, the mixture was acidified to pH 2 by adding TFA and the folded peptide was desalted and purified by preparative RP-HPLC using a linear gradient (17-37% CH_3CN in 0.1% TFA for 80 min) to obtain 5.3 mg from the previous 23 mg (23% yield).

ESI/Q-TOF Mass Spectrometry–All masses obtained during chemical synthesis were confirmed by electrospray ionization mass spectrometry using an ESI/Q-TOF mass spectrometer (Micromass, Manchester, U.K.). Peptides were mixed with 1% (v/v) formic acid / 70% (v/v) CH_3CN and data analyzed using MassLynx v3.4 software (Micromass).

Capillary Electrophoresis–Capillary zone electrophoresis (CZE) analyses were performed on a Jasco CE800 system (Jasco, Japan) equipped with a UV detector connected to a Shimadzu CR-4A recorder and a capillary (0.1 μm ID, 70 cm length, 50 cm to detector). 20 mM sodium citrate buffer (pH 2.5) was used for the analyses. Samples dissolved in migration buffer were applied hydrodynamically to the capillary (height 20 cm, 15 s) and analyses were performed with a 20 kV constant voltage drop and monitored at 210 nm.

Circular Dichroism (CD) Measurements–CD spectra were obtained on a Jasco J-725 spectropolarimeter (Jasco, Japan). The spectra were measured from 260 to 180 nm in 60% TFE, pH 7.1, at room temperature, with a 1 mm path-length cell. Data were collected at 0.1 nm with a scan rate of 100 nm/min and a time constant of 1 s. The concentration of the toxins was 30 μM, as determined by amino acid analysis. Data from 10 separate recordings were averaged and analyzed by the method of Bohm et al. (18).

Iodination of LqhαIT and Binding Assays–The toxin was radio-iodinated with bovine milk lactoperoxidase (EC 1.11.1.7, Sigma-Aldrich, Germany) using 0.7 lactoperoxidase units, 1 nmole of toxin and 0.5 mCi carrier-free $Na^{125}I$ (Amersham, UK) (19). The displacement assays were performed as previously described (19) (see supplementary information).

NMR Experiments–Synthetic δ-HXTX-Mg1a (4.7 mg) was dissolved to a final concentration of 3.7 mM in 250 μl of H_2O/D_2O (90/10; v/v) containing 50 mM NaN_3 in a susceptibility-matched microcell (Shigemi, Japan). The pH was adjusted to 2.4.

NMR spectra were recorded on a Bruker DMX-750 spectrometer. The temperature was set to 298 K. Chemical shifts were referenced to internal TSP. 2D DQF-COSY, NOESY and TOCSY experiments were performed using standard pulse sequences and phase cycling. The NOESY spectra were acquired with mixing times of 50 ms and 200 ms. The TOCSY spectrum was recorded with a spin lock time of 71 ms. The 2D spectra were recorded using time-proportional phase incrementation for quadrature detection in the F1 dimension. For water suppression, the NOESY experiments include the WATERGATE sequence, and the DQF-COSY and TOCSY experiments included selective low-power irradiation during the relaxation delay. The TOCSY and NOESY spectra were recorded with 512 (t_1) x 2K (t_2). The DQF-COSY spectrum was recorded with 512 (t_1) x 8K (t_2) for an estimation of the coupling constants. The spectra were processed using the XWIN-NMR 2.5 program (Bruker Biospin) running on an O_2 workstation (Silicon Graphics). Chemical shift assignments have been

deposited in the BioMagResBank (BMRB), accession code 11044.

Structural Calculations–Proton signal assignments were achieved using the standard strategy described by Wüthrich with the graphical software ANSIG.3.3. The DQF-COSY and TOCSY spectra gave the spin system fingerprint of the peptide. The spin systems were then sequentially connected using the NOESY spectra. Interproton distance restraints were obtained from the NOESY spectra acquired with a mixing time of 200 ms. The NOE volumes were converted into four ranges of distance restraints classified as strong (1.8–2.7 Å), medium (1.8–3.3 Å), weak (1.8–5.0 Å), and very weak (1.8–6.0 Å). The backbone $^{3}J_{\mathrm{NH\text{-}H}\alpha}$ coupling constants were estimated or directly measured from a 1D spectrum or the high-digital resolution DQF-COSY spectrum using the DECO program (Bruker Biospin). Hydrogen bonds were identified using amide-proton temperature coefficients from NOESY spectra obtained at 288 K, 298 K, 308 K, 318 K and 328 K.

The structural calculations were performed using the X-PLOR-NIH 2.9.1 program with 576 NOE-based distance restraints, which contain 207 intraresidue, 181 sequential, 60 medium-range and 128 long-range restraints. In the first stage, the starting extended strand structure was subjected to 10 ps and 1,000 steps of torsion-angle molecular dynamics at 50,000 K. The structures were then subjected to 15 ps and 1,500 steps of a slow-cooling torsion angle molecular dynamics stage in which the temperature was reduced from 50,000 K to 298 K over 250 steps. Finally, the structures were subjected to 200 steps of conjugated-gradient minimization. The initial runs for structure calculations were performed without hydrogen bond and disulfide bond restraints and the obtained structure was examined.

The structures were checked for violations of geometric and experimental restraints, and atom overlapping, using the AQUA3.2 and PROCHECK-NMR3.4 programs. Finally, a set of 20 conformers was selected based on the lowest X-PLOR energy. Structures were analyzed and visualized with the MOLMOL 2k.1 program.

Neuronal Isolation Procedures and Na_V Channel Expression–Characterization of the actions of δ-HXTX-Mg1a on native I_{Na} were performed using acutely dissociated newborn rat DRG neurons and cockroach DUM neurons from the terminal abdominal ganglia of adult male American cockroaches (*Periplaneta americana*) as previously described (20,21). Following isolation, recordings were made within 24 hours.

For expression in *Xenopus laevis* oocytes, the $rNa_V1.1$, $rNa_V1.2$, and $mNa_V1.6$ genes were subcloned into pLCT1. The $rNa_V1.3$, $rNa_V1.4$, $hNa_V1.5$, $DmNa_V1$, and tipE genes were subcloned into vectors pNa3T, pUI-2, pcDNA3.1, pGH19-13-5 and pGH19 respectively. For *in vitro* transcription, these plasmids were linearized with *Not*I. The $rNa_V1.7$/pBSTA.rPN1 and hβ_1/pGEM-HE were linearized with *Sac*II and *Nhe*I, respectively. Capped cRNAs were then synthesized from linearized plasmid using the T7 mMESSAGE-mMACHINE transcription kit (Ambion). The rβ_1/pSP64T and $hNa_V1.8$/pBSTA vectors were linearized with *Eco*RI and *Not*I respectively, and transcribed with the SP6 mMESSAGE-mMACHINE transcription kit (Ambion).

Stage V-VI oocytes were harvested from the ovarian lobes of anaesthetized female *X. laevis* frogs as described previously (22). The oocytes were injected with up to 50 nl of cRNA at a concentration of 1 ng nl^{-1} using a Drummond microinjector (Ambion). The ND96 solution used for incubating the oocytes contained (in mM): NaCl 96, KCl 2, $CaCl_2$ 1.8, $MgCl_2$ 2, HEPES-acid 5 (pH 7.4), supplemented with 50 mg l^{-1} gentamycin sulfate. Whole-cell currents from oocytes were recorded 2–5 days after injection.

Electrophysiological Studies–Voltage- or current-clamp recordings from single DRG and DUM neurons were made using the whole-cell patch-clamp technique of Hamill et al. (23). Recordings from *X. laevis* oocytes were performed using the two-electrode voltage-clamp method as described by Liman et al. (22).

Experiments were performed at constant temperature 18–24 ˚C using either an AxoPatch 200A patch-clamp amplifier or GeneClamp 500 amplifier. Current and voltage pulse protocols were generated using the pClamp software system (Molecular Devices, Sunnyvale, CA, USA). Data were digitized at 10–25 kHz, and low-pass filtered at either 1 kHz (oocytes) or 5 kHz (DRG and DUM neurons) using a 4- or 5-pole Bessel filter (–3 dB). Leakage and capacitive currents were digitally subtracted with *P-P*/4 procedures and series resistance compensation set at >80% for all patch-clamped cells to minimize voltage errors. The extracellular Na^+ concentration was reduced (see below) to minimise series resistance errors.

The voltage-clamp data recorded in this study were rejected if there were large leak currents upon seal formation or currents showed signs of

inadequate space clamping. At the commencement of each experiment, oocytes or DUM neurons exhibiting leakage currents at a holding potential of -90 mV of more than –200 nA or –600 pA, respectively, were discarded. Only cells exhibiting stable leakage currents throughout the whole experiment (with a maximal deviation of ± 10 % of initial value) were considered in the data analysis. To avoid overestimation of a potential toxin-induced shift in the current-voltage relationship as a result of inadequate voltage control when measuring large sodium currents in oocytes, only results from cells with currents lower than 1.5 μA were considered. Current-clamp data were rejected if the initial resting membrane potential was more depolarized than –45 mV.

Recording Solutions–DRG neurons were perfused with an external solution containing (in mM): Na acetate 30, $MgCl_2$ 1, $CaCl_2$ 1.8, Cs acetate 5, KCl 5, D-glucose 25, HEPES-acid 5, TEA-Br 100, $CdCl_2$ 0.5, 4-AP 1 with the pH adjusted to 7.4 with 1 M TEA-OH. Recordings were performed using micropipettes filled with a solution containing (in mM): CsF 135, Na acetate 8, HEPES-acid 5, with the pH adjusted to 7.0 with CsOH. The osmolarity of internal and external solutions was adjusted to 300–305 mOsmol litre^{-1} with sucrose, prior to use, to reduce osmotic stress. Pipettes with resistances of 0.8–2 MΩ were used for recording I_{Na} from DRG neurons.

For voltage-clamp experiments, DUM neurons were perfused with an external solution consisting of (in mM): NaCl 90, CsCl 5, $CaCl_2$ 1.8, 4-AP 5, TEA-Cl 50, verapamil 0.01, $NiCl_2$ 0.1, $CdCl_2$ 1, HEPES-acid 10, pH adjusted to 7.4 with HCl. Micropipettes were filled with an internal solution consisting of (in mM): CsF 135, $MgCl_2$ 1, NaCl 34, ATP-Na_2 3, EGTA 5, HEPES-acid 10, pH adjusted to 7.35 with CsOH. For current clamp experiments, DUM neurons were perfused with an external solution consisting of (in mM): NaCl 190, KCl 3.1, $CaCl_2$ 5, $MgCl_2$ 4, HEPES-acid 10, with the pH adjusted to 7.4 with NaOH. Micropipettes were filled with an internal solution consisting of (in mM): K gluconate 160, KF 10, ATP-Mg 1, $CaCl_2$ 0.5, NaCl 15, $MgCl_2$ 1, EGTA 10, HEPES-acid 10, with the pH adjusted to 7.4 with KOH. The osmolality of all solutions was adjusted to 400 mOsm litre^{-1} with sucrose. Pipettes with resistances of 1.2–2 MΩ were used for recording currents from DUM neurons.

Oocytes were perfused with ND96 solution. Voltage and current electrodes were filled with 3 M KCl and resistances were <1 MΩ.

Voltage- and Current-clamp Recordings–In DRG neurons, the predominant TTX sensitivity of the Na_v channels present in each cell was determined using a modified steady-state Na_v channel inactivation (h_∞) voltage-clamp protocol (24,25). This takes advantage of the separation of h_∞ curves for TTX-sensitive and TTX-resistant Na_v channels (26). Only those found to have less than 10% TTX-resistant I_{Na} were used for TTX-sensitive experiments. Of the remaining cells, those expressing sufficiently large TTX-resistant I_{Na} were used for experiments by perfusing with external solution containing 200 nM TTX.

To determine the effect of the toxin on fast inactivation, currents were recorded in the absence, and presence, of a range of toxin concentrations. The action of the toxin on fast inactivation was assayed by measuring the late current remaining at 50 ms (I_{50ms}) for DRG and DUM neurons, or 30 ms for oocytes, as a fraction of peak current (I_{pk}). Currents were elicited by test potentials to –10 mV in DUM and DRG neurons or at depolarizing test potentials corresponding to maximal activation in oocytes (ranging from –10 to +10 mV). Test potentials were applied at 10 s (DRG and DUM) or 5 s (oocytes) intervals. The normalised late current ratio (eg. I_{50ms} / I_{pk}) gives the fractional probability for Na_V channels not to be inactivated at the end of the test pulse. The concentration dependence for removal of inactivation was measured by plotting the normalised late current as a function of toxin concentration according to the following Hill equation (Eq. 1):

$$\frac{I_{50ms}}{I_{pk}} = \frac{100}{1+\left(\frac{EC_{50}}{[\text{toxin}]}\right)^{n_H}}$$

where EC_{50} is the concentration at half maximal inhibition of fast inactivation, [toxin] is the toxin concentration and n_H is the Hill coefficient.

The effect of δ-HXTX-Mg1a on the voltage-dependence of Na_v channel activation was determined using depolarizing test pulses from –90 to +70 mV for 50 ms, in 5-mV (oocytes) or 10-mV (DRG and DUM) steps. The values for sodium conductance (g_{Na}) were calculated according to the equation (Eq. 2):

$$g_{Na} = \frac{I_{Na}}{(V - V_{rev})}$$

where I_{Na} is the absolute value of the sodium current at a given test potential (V) and V_{rev} is the reversal potential. The values of g_{Na} and V–V_{rev} were then fitted to a Boltzmann equation (Eq. 3):

$$\frac{g_{Na}}{g_{max}} = \frac{1}{1+\exp[(V_{1/2}-V)/k_m]}$$

where g_{max} is maximal g_{Na}, $V_{1/2}$ is the half- maximal conductance, k_m is the slope factor.

To determine the effect of *δ*-HXTX-Mg1a on the voltage-dependence of steady-state Na_V channel fast inactivation (h_∞) a two-pulse protocol with a 0.5-ms interpulse interval was applied. This consisted of a 500 ms or 1 s conditioning prepulse (V_{cond}), in which the holding potential of –90 mV was stepped to potentials ranging from –130 up to +20 mV in 5-mV (oocytes) or 10-mV (DRG and DUM) increments, followed by a 50-ms test pulse (V_{test}) to –10 mV in DRG or DUM neurons, or potentials corresponding to maximal activation in oocytes. Pulses were applied every 10 s. Data were normalised to the maximum peak control I_{Na} and fitted using a Boltzmann equation (Eq. 4):

$$h_\infty = \frac{1-C}{1+\exp[(V-V_{1/2})/k_h]} + C$$

where $V_{1/2}$ is the voltage at half-maximal inactivation, k_h is the slope factor, V is the test voltage, and C is a constant or non-inactivating fraction (usually zero in controls).

The effect of the toxin on the rate of recovery from Na_V channel inactivation was examined by applying a standard two-pulse protocol with a variable interpulse interval (ΔT). A 50-ms conditioning prepulse (V_{cond}) was applied from a holding potential of –90 mV to –10 mV, followed by a 50-ms test pulse (V_{test}), with an interpulse interval ranging between 0.5 ms and 4 s.

Mathematical curve fitting was accomplished using GraphPad Prism version 5.00 for Macintosh (GraphPad Software, San Diego CA, USA). All curve-fitting routines were performed using non-linear regression analysis employing a least squares method. Comparisons of two sample means were made using a paired Student's *t*-test. Multiple comparisons were assessed by repeated measures ANOVA with a Bonferroni's multiple comparison post-hoc test. A test was considered to be significant when $P < 0.05$. All data are presented as mean ± standard error of the mean (SEM) of *n* independent experiments.

RESULTS

Peptide Synthesis and Characterization–*δ*-HXTX-Mg1a was synthesized with its *C*-terminus as the free carboxyl, as observed for the native toxin by mass spectrometry and from the cDNA encoding gene (10). The structural identity between the synthetic and native toxins was verified by ESI/Q-TOF MS and CZE (supplemental Fig. S1 and Table S1). In a co-injection experiment, native *δ*-HXTX-Mg1a and synthetic *δ*-HXTX-Mg1a coeluted in a single sharp peak (supplemental Fig. S1*A*). Moreover, the CD spectra of synthetic and native *δ*-HXTX-Mg1a superimposed indicating that their secondary structures were similar. Both native and synthetic *δ*-HXTX-Mg1a were able to displace the binding of ^{125}I-Lqh*α*IT from insect Na_V channels in cockroach synaptosomes with similar IC_{50} values (supplemental Fig. S1*B*-*C*).

NMR Spectroscopy–Sequence specific ^{1}H resonance assignments for all residues observed were established using standard methods (27). NOE cross peaks were converted to distance restraints for structural calculation. From NMR experiments, 582 distance constraints and 22 dihedral angle constraints were used for the structural calculations. The total of 582 distance restraints included 576 NOE constraints and 6 hydrogen bonds (Fig. 1*B*). In addition, disulfide bond constraints were also used (Cys^1-Cys^{15}, Cys^8-Cys^{20}, Cys^{14}-Cys^{31} and Cys^{16}-Cys^{43}). Simulated annealing calculations were started from an extended structure and 20 structures were selected with the lowest XPLOR energy, which had no ≥ 0.4 Å NOE distance violations and no ≥ 5.0° angle violations from 100 structures obtained at the final calculation (28). Structural statistics for these 20 converged structures are summarized in Table 1. Figure 2*A* shows a stereoview of the best-fit superposition of the backbone atoms (N, C, C^α and O) for 20 converged structures. The root-mean-square deviations with respect to the mean coordinate positions are 0.483 Å for backbone atoms and 1.178 Å for all heavy atoms of the disulfide-rich structured region (Gly^2-Ala^{23} and Gln^{28}-Glu^{32}), excluding the non-structured loop (Trp^{24}-Gln^{27}) and *C*-terminal (Arg^{33}-Cys^{43}) regions. Analysis of the 20 structures using PROCHECK-NMR and AQUA reveals that 95.1% of the backbone dihedral angles for the structured region lie in the most favored and additional allowed regions of the Ramachandran plot (29).

Six protons from amide groups were identified to form hydrogen bonds according to the amide proton temperature coefficients (Supplemental Fig. S2). If the hydrogen bond was in agreement with amide temperature coefficients (> –4.6 ppb/K), and a hydrogen bond acceptor and an oxygen atom of the backbone was within 2.6 Å of the amide-proton,

the amide-proton was identified as a donor of the hydrogen bond. Hydrogen bond acceptors for all the protons were unambiguously determined from preliminary structure calculations. These restraints were then used in the following stage of structure calculations ($1.8 \leq d \leq 2.12$ Å for NH_i-O_j and $2.7 \leq d \leq 3.2$ Å for N_i-O_j) (30).

Twenty-two dihedral angles estimated from the $^3J_{NH\text{-}H\alpha}$ values were used as) angle constraints within the range of –90° and –40° for $^3J_{NH\text{-}H\alpha} < 5.5$ Hz (Ala^6, Trp^7, Cys^{15}, Trp^{24}, Cys^{31}, Arg^{33}, Lys^{36}, Phe^{39}), and between –160° and –80° for $^3J_{NH\text{-}H\alpha} > 8$ Hz (Ser^3, Cys^8, Lys^9, Cys^{14}, Tyr^{18}, Asn^{19}, Cys^{20}, Ala^{23}, Asn^{26}, Gln^{28}, Ser^{29}, Glu^{32}, Trp^{35}, Glu^{42}) following standard parameterization (31) (Fig. 1*B*).

From the results of initial runs without using the disulfide bridge restraints, the disulfide patterns of Cys^1-Cys^{15} and Cys^{16}-Cys^{43} were unambiguously determined. Analyzing the distances between Sγi and Sγj of the remaining four cysteines, three types of disulfide patterns were possible (pattern I: Cys^8-Cys^{14}, Cys^{20}-Cys^{31}; pattern II: Cys^8-Cys^{31}, Cys^{14}-Cys^{20}; and pattern III: Cys^8-Cys^{20}, Cys^{14}-Cys^{31}). Three sets of structure calculations were performed with these possible restraints. The energy minimization was done *in vacuo* with the GROMOS96 43B1 parameters set, without reaction field (32), to determine the lowest energy state and thus the most stable disulfide pattern of *δ*-MSTX-Mg1a. Energy computations were done with the GROMOS96 (32) implementation of Swiss-PdbViewer (33). Total energy calculations for pattern I, II and III were –693.5, –892.7 and –1523.4 kJ/mol respectively, therefore unambiguously determining the remaining disulfide bridge patterns as Cys^8-Cys^{20} and Cys^{14}-Cys^{31}. These disulfide bridges, along with Cys^1-Cys^{15} form an ICK motif (Fig. 2*D*), and a pattern (I-IV, II-VI, III-VII, V-VIII) identical to other *δ*-HXTX-1 family members (14,15)Fig. 1*A*).

Description of the three-dimensional structure– Figure 2*A* shows the best-fit superposition of the backbone atoms (N, C^{α}, and C) for the 20 converged structures of *δ*-HXTX-Mg1a. The three-dimensional structure of *δ*-HXTX-Mg1a comprises several well-defined regions, consisting of an antiparallel *β*-sheet (strand 1: Asn^{19}-Ala^{23}, strand 2: Gln^{28}-Glu^{32}) with some secondary structural elements (Figs. 1*B* and 2*B*). We identified turns by the standard definition that the distance between $C\alpha_i$ and $C\alpha_{i+3}$ is less than 7 Å (34,35). The two turns involve Ser^3 to Ala^6 (turn 1) and Cys^{15} to Tyr^{18} (turn 2). The average dihedral angles for residues at positions *i*+1 and *i*+2 are follows: $_2$ = –40°, φ_2 = 122° for Lys^4 and $_3$ = 57°, φ_3 = 84° for Arg^5, $_2$ = –45°, φ_2 = 128° for Cys^{16} and $_3$ = 98°, φ_3 = –2° for Gly^{17}. Turn 1 is classified as a miscellaneous type IV *β*-turn. There is no hydrogen bonding in this turn conformation. Arg^5 in turn 1 shows a positive φ_3 value, since non-glycine residues at position *i*+2 are rare in type II *β*-turns and furthermore arginine shows low turn potential. Turn 2 is assigned as a typical type II *β*-turn ($\beta_{\gamma L}$). In this turn, the Cys^{15} oxygen atom forms hydrogen bonding with the Tyr^{18} amide-proton (Fig. 1*B*). The region Trp^{24} to Gln^{27} is not well defined by the NMR data.

Electrophysiological Studies on Mammalian Na_V Channels–The effects of *δ*-HXTX-Mg1a were initially examined on neonatal rat DRG neurons as these were employed in the original characterization of *δ*-HXTX-1 and *δ*-AOTX-Mb1a toxins (36-38). Rat DRG neurons express two types of Na_V channel currents, TTX-sensitive (mainly $Na_V1.1$, $Na_V1.6$ and $Na_V1.7$) and TTX-resistant ($Na_V1.8$ and $Na_V1.9$) (26,39). Like *δ*-HXTX-1 toxins, *δ*-HXTX-Mg1a slowed inactivation of TTX-sensitive I_{Na} in DRG neurons (Fig. 3*A*). This was observed as a sustained current in the presence of the toxin during depolarizing test potentials to –10 mV in which I_{Na} are fully inactivated in the absence of toxin. This is most likely the result of a marked slowing of transitions between open and open-inactivated states. The maximum degree of slowing of inactivation after 50 ms was 26.3 ± 4.4% (n = 7) of control peak I_{Na} at 300 nM, with an EC_{50} of 46 nM (Fig 3*E*). This steady-state current was completely blocked by 100 nM TTX indicating that it is mediated exclusively via Na_V channels (data not shown). In parallel, the peak I_{Na} amplitude recorded at –10 mV transiently increased but after 5 min perfusion was slightly reduced by 6.6 ± 11.0% (n = 7).

Similar to *δ*-HXTX-1 toxins (37,38), this effect was accompanied by a modest 10 mV hyperpolarizing shift in the threshold, but not the midpoint ($V_{1/2}$), of Na_V channel activation (Fig. 3*C*). Furthermore, *δ*-HXTX-Mg1a, at concentrations up to 1 *μ*M, failed to modulate TTX-resistant I_{Na} (Fig. 3*B* and *D*). Unlike *δ*-HXTX-1 toxins, however, the effect to slow Na_V channel inactivation in TTX-sensitive DRG neurons was almost completely reversible after washing with toxin-free solution with a τ_{on} of 84.9 ± 18.4 s and τ_{off} of 81.5 ± 9.2 s (n = 5).

Given the potent action of *δ*-HXTX-Mg1a on DRG neurons, we then assayed the effect of the toxin on eight mammalian Na_V channel clones

($Na_V1.1/\beta_1$-$Na_V1.8/\beta_1$) by analyzing g_{Na}/V relationships and steady-state inactivation. Effects of the toxin on $Na_V1.9$ channels were not investigated as this channel subtype currently fails to express in standard heterologous systems (40). Addition of *δ*-HXTX-Mg1a (up to 5 μM) to the bath medium produced a marked slowing of I_{Na} inactivation with a rank order in magnitude of $Na_V1.6/\beta_1 > Na_V1.1/\beta_1 > Na_V1.3/\beta_1$. However with $Na_V1.2/\beta_1$ and $Na_V1.7/\beta_1$ there were only weak effects to slow I_{Na} inactivation (Fig. 4*A* left-hand panels and supplemental Table 2*S*). These effects were accompanied by ~20% increase in peak I_{Na} amplitude with $Na_V1.6/\beta_1$ and $Na_V1.1/\beta_1$ channels but less significant changes with the remaining channel clones (supplemental Table 2*S*).

The above effects were accompanied by only weak hyperpolarizing shifts in the voltage-dependence of activation (g_{Na}) to a maximum $\Delta V_{1/2}$ of –8.9 mV for $Na_V1.3/\beta_1$ channels (Fig. 4*A* right-hand panels). In contrast, the toxin failed to slow I_{Na} inactivation of $Na_V1.4/\beta_1$, $Na_V1.5/\beta_1$ or $Na_V1.8/\beta_1$ channels at concentrations up to 5 μM (Fig. 4*B*). This lack of activity on $Na_V1.8/\beta_1$ channels is consistent with the lack of effects on TTX-resistant I_{Na} in DRG neurons that express both $Na_V1.8$ and $Na_V1.9$.

In the mammalian Na_V channel clones, steady-state inactivation (h_∞) in the absence of toxin was best described by a single Boltzmann function. *δ*-HXTX-Mg1a (5 μM) caused a strong –19.7 mV hyperpolarizing shift in the voltage at half-maximal inactivation ($V_{1/2}$) of $Na_V1.3/\beta_1$, but only weak non-significant shifts in $V_{1/2}$ in $Na_V1.1/\beta_1$, $Na_V1.2/\beta_1$, $Na_V1.6/\beta_1$ and $Na_V1.7/\beta_1$ channels of less than –4 mV (Fig. 4*A* right-hand panels). Moreover, in the presence of *δ*-HXTX-Mg1a steady-state inactivation became incomplete, causing the appearance of a non-inactivating component at prepulse test potentials more depolarized than –40 mV, an effect previously noted with *δ*-HXTX-1 toxins (37,38). This non-inactivating component was up to 27 ± 10% (n = 5) of peak current in the case of the $Na_V1.1/\beta_1$ channel (determined from *C* in Eq. 4) with a rank order in magnitude of $Na_V1.6/\beta_1 > Na_V1.1/\beta_1 > Na_V 1.3/\beta_1 >> Na_V1.2/\beta_1 > Na_V1.7/\beta_1$ (Fig. 4*A* right-hand panels). This was sufficient to induce significant changes in the slope factor, k_h, in all Na_V channel clones except $Na_V1.2/\beta_1$. Although time-dependent shifts in h_∞ have been demonstrated in patch-clamp configurations (41) these are unlikely to account for the observed changes given the magnitude of the shift in $Na_V1.3/\beta_1$ and the absence of a non-inactivating component in controls.

Electrophysiological Studies on Insect Na_V Channels–In contrast to the clear effects, but modest potency, of the toxin on mammalian Na_V channel gating and kinetics, *δ*-HXTX-Mg1a showed high affinity for the *Drosophila* Na_V channel clone $DmNa_V1$/TipE. This was evident firstly by a concentration-dependent increase in control peak I_{Na} amplitude up to a maximum of 290 ± 37% at 1 μM (n = 5; Fig. 5*C*). This was most likely the result of the marked concentration-dependent slowing of fast inactivation (Fig. 5*A* and *C*) with an EC_{50} of 22.8 nM (Fig. 5*H*). Importantly *δ*-HXTX-Mg1a completely removed fast inactivation at concentrations of 1 μM (Fig. 5*C*). This was accompanied by up to a 21.8 mV hyperpolarizing shift in $DmNa_V1$/TipE channel activation at 1 μM (n = 3, Fig. 5*D*). At a concentration of 15 nM, *δ*-HXTX-Mg1a also caused steady-state $DmNa_V1$/TipE channel inactivation to become incomplete at prepulse test potentials more depolarized than –50 mV (non-inactivating component C = 49.2 ± 0.3%, Fig. 5*B*). At higher concentrations, the toxin completely prevented channel inactivation (Fig. 5*D*).

To further probe the mode of action and insect-selectivity of *δ*-HXTX-Mg1a we assayed the toxin on cockroach DUM neurons, previously employed in the characterisation of *δ*-HXTX-Hv1a (42). Like *δ*-HXTX-Hv1a, *δ*-HXTX-Mg1a produced a potent time- and concentration-dependent slowing of I_{Na} inactivation (Fig. 5*E* and *H*). Maximum slowing after 50 ms was 46.1 ± 4.5% (n = 10) of control peak I_{Na} at 300 nM *δ*-HXTX-Mg1a (Fig. 5*E*). The EC_{50} for the slowing of inactivation in DUM neurons was 823 pM, *ca*. 56-fold lower than in DRG neurons (Fig. 5*H*). Hence, although this toxin is not insect-specific, it shows a marked selectivity for insect Na_V channels. The toxin also caused 14.3 and 13.5 mV hyperpolarizing shifts in the $V_{1/2}$ of Na_V channel activation and steady-state inactivation, respectively (Fig. 5*F*).

In DUM neurons, the slowing of inactivation described above was accompanied initially by a slight increase in the peak I_{Na}. This effect would reach a maximum after *ca*. 70 s followed immediately by a decrease in peak and late I_{Na} amplitude (Fig. 5*E*). If depolarising test pulses were abolished for 2 min after reaching steady-state toxin effects (e.g. after 4–5 min perfusion), peak and late I_{Na} amplitude increased markedly (Fig. 5*G*, trace marked '120 s'). If depolarising test pulses

(Δt = 10 s) were then reapplied, peak and late I_{Na} amplitude would decline back to steady-state levels within *ca*. 1 min (Fig. 5*G*, trace marked '180 s'). This effect may result from a slowed rate of recovery from fast inactivation or a voltage-dependent dissociation of the toxin from the channel. To test these possibilities we firstly assessed the effect of *δ*-HXTX-Mg1a (30 nM) on the rate of recovery from inactivation. While the toxin markedly increased repriming kinetics at interpulse intervals less than 3 ms, presumably reflecting a more rapid transition from open to closed states, the major effect of the toxin was to prolong the rate of recovery from fast inactivation at interpulse intervals greater than 3 ms, reflecting a slowed transition between closed-inactivated and closed states (Fig. 6*A*). This action resulted in a use-dependent decrease in peak I_{Na} amplitude during repetitive stimulation at 30 Hz (Fig. 6*B*).

To determine whether the effect of the toxin was dependent on the holding potential the amplitude of the toxin-modified I_{Na} measured at the end of the test pulse was compared to peak I_{Na} at hyperpolarized holding potentials. In comparison with currents recorded at –90 mV, the fraction of the sustained I_{Na}, measured at the end of the 50 ms depolarizing test pulse (I_{50ms}), compared with the peak I_{Na} amplitude (I_{pk}) was not significantly increased except at −150 mV ($P < 0.05$, $n = 7$, Fig. 6*C*). In addition, to test if depolarising pulses could cause dissociation of the toxin, post-pulses up to +200 mV were applied immediately following a test pulse to –10 mV from –90 mV every 2 s. At this stimulation frequency there was some initial rundown in peak and late I_{Na} amplitude but the depolarizing post-pulses failed to cause any significant decrease in fractional I_{50ms}/I_{pk} compared to data recorded in the absence of the post-pulse ($P > 0.05$, $n = 5$; Fig. 6*D*)

To investigate the effects of the toxin on membrane excitability, DUM neurons were held under current-clamp conditions and action potentials evoked by depolarizing current pulses. *δ*-HXTX-Mg1a (100 nM) initially produced a prolongation of the repolarizing phase of the action potential (Fig. 7*A*). The falling phase of the action potential developed a broad shoulder in the last two-thirds of the repolarization phase (Fig. 7*A*). This caused a suppression of the afterhyperpolarization and an increase in spike duration resulting in 'plateau' action potentials (Fig. 7*A*-*C*). Although a small depolarization of 3.1 ± 0.6 mV ($n = 5$) was observed, neither resting membrane potential (RMP) nor spike amplitude were significantly altered. Applying artificial hyperpolarization to a level 20–40 mV more negative than the RMP facilitated the appearance of these plateau potentials. In addition, the duration of plateau potentials were heavily influenced by the stimulation frequency such that the duration increased from *ca*. 70 ms at a RMP of –60 and stimulus interval of 10 s (Fig 7*A*) to *ca*. 300 ms at stimulus intervals of 1 min at a RMP held at –90 mV (Fig. 7*C*). Interestingly, 100 nM *δ*-HXTX-Mg1a co-applied with 500 μM 3-4 diaminopyridine (3,4-DAP), a K_V channel blocker, markedly prolonged the action potential duration to *ca*. 150 ms at –60 mV (Fig. 7*D*) and *ca*. 800 ms at –90 mV (Fig. 7*E*). In this case, the action potential duration was more than 80-fold longer than with 3,4-DAP applied alone.

As previously described DUM neurons are spontaneously active (43). At resting membrane potentials, most DUM neurones were capable of generating repetitive action potentials with firing frequencies of 31 ± 4.6 Hz ($n = 4$; Fig. 7*F*). In the presence of 100 nM *δ*-HXTX-Mg1a, repetitive plateau action potentials of *ca*. 70 ms duration would also occur spontaneously, albeit with a much reduced firing frequency of 3.2 ± 0.6 Hz ($n = 4$; Fig. 7*G*). However, when the membrane potential was hyperpolarized to –80 mV, spontaneous plateau action potential duration increased up to *ca*. 500 ms but firing frequency was still low at 0.7 ± 0.2 Hz ($n = 4$; Fig. 7*H*). Using a ramp current from –80 mV at 0.2–0.4 nA/s there was also a –26 ± 2.0 mV shift in the threshold of spontaneous firing from –44.6 ± 4.0 mV in controls to –70.6 ± 3.5 mV ($n = 7$) in the presence of 100 nM *δ*-HXTX-Mg1a.

DISCUSSION

Actions on Na_V channel gating

In all cases, *δ*-HXTX-Mg1a modulated channel gating and kinetics in a similar fashion to other *δ*-HXTX-1 toxins by causing: (i) a slowing/removal of Na_V channel inactivation typically associated with an increase in peak Na_V channel currents, (ii) a hyperpolarizing shift in the voltage dependence of channel activation, and (iii) a hyperpolarizing shift in the voltage dependence of steady-state inactivation. In insect neurons, further characterization revealed that the toxin (iv) slowed Na_V channel repriming kinetics, and (v) caused a use-dependent reduction in I_{Na} amplitude.

The toxin-induced increase in peak I_{Na} seen with $DmNa_V1$ and to a lesser extent in DUM neurons, $rNa_V1.1$, $rNa_V1.3$ and $Na_V1.6$, was in general well correlated with the magnitude of the sustained

current at the end of the depolarizing test pulse. This increase in peak I_{Na} can be explained by a delay in Na_V channel fast inactivation from open to open-inactivated states. In contrast, δ-HXTX-Mg1a did not slow I_{Na} inactivation as markedly in $Na_V1.2$, or $Na_V1.7$ and therefore did not appreciably increase peak I_{Na} amplitude. This slowing of the transition from open to open-inactivated states also generated a non-inactivating component in the steady-state inactivation curve. This occurred at prepulse test potentials more depolarized than –40 mV, an effect previously noted with δ-HXTX-1 toxins (37,38). This is the result of a more rapid rate of recovery from fast inactivation when test pulses are separated by less than 3 ms. This reflects a higher proportion of transitions between open and closed states than open-inactivated to closed states via a closed-inactivated intermediate.

The present study demonstrates that δ-HXTX-Mg1a displays differential Na_V channel subtype specificity for $Na_V1.1/\beta_1$, $Na_V1.3/\beta_1$, and $Na_V1.6/\beta_1$ channels. This is consistent with its action on TTX-sensitive I_{Na} in rat DRG neurons that express mainly $Na_V1.1$, $Na_V1.3$ and $Na_V1.7$ channels (39). Importantly, however, δ-HXTX-Mg1a showed considerably higher affinity for invertebrate *Drosophila* $DmNa_V1$ and cockroach Na_V channels. Differences in the EC_{50} of δ-HXTX-Mg1a for dipterans ($DmNa_V1$) *vs*. orthopterans (DUM neurons) have been previously noted for Lqh3 and δ-HXTX-Hv1a with cockroach *vs*. locust Na_V channels (11,44).

In cockroach DUM neurons, the slowing of Na_V channel inactivation by δ-HXTX-Mg1a induced the development of prolonged plateau action potentials. This was accompanied by spontaneous repetitive firing as a result of a hyperpolarizing shift in the threshold of action potential generation due to a negative shift in the voltage-dependence of Na_V channel activation. The reduction in firing frequency observed in tonically active neurons probably reflects the reduced rate of recovery from fast inactivation at interpulse intervals greater than 3 ms, presumably resulting from a slowing of the frequency of transition between the closed-inactivated and closed states. This is supported by the use-dependent decrease in I_{Na} amplitude during repetitive pulses. Interestingly, in DUM neurons, δ-HXTX-Mg1a produced greater inhibition of I_{Na} inactivation (Fig. 7*I*), with resultant prolongation of action potential duration, when the membrane potential was held at more hyperpolarized potentials (Fig. 8*H*). This suggests that the toxin partially dissociates from the channel at more depolarized potentials. Voltage-dependent dissociation of bound toxins from vertebrate Na_V channels has already been demonstrated with scorpion and sea anemone toxins (9,11,45,46) and has also been observed with δ-HXTX-Hv1a on insect DUM neurons (42). However there was no indication of any depolarization-dependent dissociation of toxin from DUM neurons using hyperpolarized holding potentials or depolarizing post-pulse protocols.

Comparison with orthologous δ-HXTX-1 toxins

These actions on TTX-sensitive Na_V channel subtypes in rat DRG and insect DUM neurons resemble the effects of other spider δ-HXTX-1 toxins, with which δ-HXTX-Mg1a shares some sequence homology (37,38,42). In contrast to δ-HXTX-1 toxins, however, δ-HXTX-Mg1a is more efficacious on insect rather than mammalian Na_V channel subtypes, including markedly different actions on repriming kinetics and use-dependent activity (this study and (10). δ-HXTX-Mg1a therefore shows greater similarity in its phyla-selective actions with scorpion α-like toxins. Like δ-HXTX-Mg1a, α-like toxins are toxic by direct injection into rat brain but fail to compete for site-3 on rat brain synaptosomes (9). Rat brain synaptosomal membranes are rich in mainly $rNa_V1.2/1.2a$ (78%) and $rNa_V1.1$ (15%) (47). Consistent with a lack on inhibition of ^{125}I-Lqh2 binding to site-3 in rat brain synaptosomes, δ-HXTX-Mg1a showed only weak effects on $Na_V1.2/\beta_1$ at 5 μM. In addition, the toxin had even weaker activity on $Na_V1.7/\beta_1$ and no activity on $Na_V1.4/\beta_1$, $Na_V1.5/\beta_1$ and $Na_V1.8/\beta_1$ channels (Fig. 4*A*). Although there is currently no reliable expression system for $Na_V1.9$ channels, the lack of effect of δ-HXTX-Mg1a on TTX-resistant I_{Na} in DRG neurons would indicate that δ-HXTX-Mg1a does not have any appreciable affinity for this channel subtype.

Scorpion α-like toxins, similar to δ-HXTX-Mg1a, specifically target $Na_V1.1$, $Na_V1.3$ and $Na_V1.6$ channels (48). Indeed the lethal actions of δ-HXTX-Mg1a, when injected intracranially, most likely results from its action on these channels and not $Na_V1.2$. However, in the present study δ-HXTX-Mg1a was not active on $Na_V1.4/\beta_1$ which α-like, α-insect and anti-mammalian α-toxins, specifically target (49). Moreover, it was only weakly active on $Na_V1.7/\beta_1$ which the novel scorpion toxin OD1 specifically targets (50). δ-HXTX-Mg1a is therefore unique from scorpion α-toxins in that it does not target $Na_V1.2$, $Na_V1.4$ or $Na_V1.7$ channels with high affinity.

Inhibitory cystine knot structural motif

δ-HXTX-Mg1a shows sequence homology with *δ*-HXTX-1 family peptides and *δ*-MSTX-Mb1a (Fig. 1*A*). Indeed, the disulfide bonding arrangement of *δ*-HXTX-Mg1a was determined from the NMR data and found to be Cys(I-IV), Cys(II-VI), Cys(III-VII) and Cys(V-VIII), the same as *δ*-HXTX-Hv1a and *δ*-HXTX-Ar1a (14,15). Like *δ*-HXTX-1 family peptides, *δ*-HXTX-Mg1a also conforms to an ICK motif (8). The ICK motif consists of double- or triple-stranded antiparallel *β*-sheets connected by three disulfide bonds, which forms a small stable globular domain and has been observed in a variety of scorpion, spider, cone snail and snake toxins (16). Specifically, *δ*-HXTX-Mg1a comprises a double-stranded antiparallel *β*-sheet and a core region (Gly^{2}-Ala^{23}, Gln^{28}-Glu^{32}) (Fig. 2*B*). The unstructured C-terminus (Arg^{33}-Cys^{43}) is most likely the result of a lack of medium- and long-range NOE constraints (Fig. 2*A*).

Structure-function relationships

Given that *δ*-HXTX-Mg1a has a similar solution structure to *δ*-HXTX-1 toxins (Fig. 2*C*) and comparable actions on Na_V channel gating and kinetics, we posited that *δ*-HXTX-Mg1a might also share key residues important for binding to their Na_V channel target. Figure 8(*A*-*C*) shows a comparison of residues that are conserved in spider *δ*-toxins targeting site-3 (14,15). A number of residues of these spider toxins are oriented in a similar fashion due to the sequence and structural homology between *δ*-HXTX-Mg1a and *δ*-HXTX-1 toxins (Figs. 1*A* and 2*C*). A cluster of positively charged residues of *δ*-HXTX-Mg1a (Lys^{4}, Arg^{5} and Arg^{33}) appears in a similar position on the surface of *δ*-HXTX-Hv1a and *δ*-HXTX-Ar1a (Lys^{3}, Lys^{4} and Arg^{5}). The positively charged Lys^{9} of *δ*-HXTX-Mg1a also seems to be oriented similarly to Lys^{10} of *δ*-HXTX-Hv1a and *δ*-HXTX-Ar1a, while aromatic residues Trp^{7} and Tyr^{22} are conserved in all these spider toxins. Finally, *δ*-HXTX-Mg1a possesses Ser^{6} in the same position as the nonpolar Asn^{6} of the *δ*-HXTX-1 toxins. However, other variations in the sequence of *δ*-HXTX-Mg1a are most likely responsible for the dramatic loss in affinity for $rNa_V1.2$ observed in ^{125}I-Lqh2 binding experiments (10), and the present voltage-clamp experiments (Fig. 4*A*). In particular, the addition/removal of charged-side chains at positions 3, 10-12, 19, 34, 36, 40-43 are dramatically different to the corresponding residues in *δ*-HXTX-1 toxins.

Site-3 toxins are proposed to slow the fast inactivation of Na_v channels by preventing the outward movement of the S4 segments (6). *δ*-HXTX-Mg1a has been previously shown to compete with the scorpion *α*-insect toxin Lqh*α*IT at subpicomolar concentrations for binding to insect site-3 (10). Recently, extensive mutagenesis studies have identified the pharmacophore of Lqh*α*IT (51). Figure 8*E* shows the critical residues in Lqh*α*IT form a functional surface composed of two domains; the NC-domain and core-domain. The positively charged residues of Lys^{4}, Arg^{5}, and Arg^{33} in *δ*-HXTX-Mg1a, are oriented similarly to Lys^{8}, Arg^{58}, and Lys^{62} in the NC-domain of Lqh*α*IT. The aromatic Trp^{7} and Tyr^{22} and basic Lys^{9} residues of *δ*-HXTX-Mg1a occupy similar positions to Phe^{17}, Trp^{38}, and Arg^{18} in the core-domain of Lqh*α*IT. These aromatic residues in *δ*-HXTX-Mg1a are also present in *δ*-HXTX-1 toxins. Despite these topologically similar residues, *δ*-HXTX-Mg1a and *δ*-HXTX-1 toxins are smaller in bulk than scorpion *α*-toxins and lack aliphatic residues corresponding to the bioactive Ile^{57} and Val^{59} residues of Lqh*α*IT. Indeed, *δ*-HXTX-Mg1a shows the greatest similarity in phyla-selectivity to scorpion *α*-like toxins eg Lqh3. Results from a mutagenesis study suggest that the core-domain of Lqh3 plays an important role in interaction with the receptor site and its toxin selectivity (52). Aromatic (Phe^{17}, Phe^{39}), positively charged (His^{15}), and aliphatic residues (Pro^{18} and Leu^{45}) were assigned to the bioactive surface in Lqh3. Importantly, the aliphatic Val^{21} and Ala^{23} of *δ*-HXTX-Mg1a are oriented similarly to those of Lqh3. The core-domain of *δ*-HXTX-Mg1a therefore seems to be involved in hydrophobic-aromatic interactions and play a role in its phyla-selectivity, although this awaits experimental confirmation.

In conclusion, while peptide neurotoxins binding with site 3 on Na_V channels are known to possess phyla-selectivity, our present study highlights a novel feature of *δ*-HXTX-Mg1a, namely target-selectivity for distinct Na_V channel subtypes. This discriminating activity of the spider toxin is somewhat unexpected given that, like homologous *δ*-HXTX-1 toxins, it interacts with both mammalian and insect Na_V channels. The effects of *δ*-HXTX-Mg1a on $DmNa_V1$/TipE, $Na_V1.1/\beta_1$, $Na_V1.3/\beta_1$, and $Na_V1.6/\beta_1$ channels as opposed to the limited or lack of activity on $Na_V1.2/\beta_1$, $Na_V1.4/\beta_1$, $Na_V1.5/\beta_1$, $Na_V1.7/\beta_1$, $Na_V1.8/\beta_1$, and $Na_V1.9/\beta_1$ channels is remarkable because it represents the first exhaustive characterisation of a selective interaction of any peptide neurotoxin across the complete range of Na_V channel subtypes.

Our findings indicate that specific insect and mammalian Na_V channel subtypes can be pharmacologically discriminated by their sensitivity to *δ*-HXTX-Mg1a as has only been partially described for scorpion *α*-toxins, sea anemone and other spider toxins (53,54). This should provide new tools to study the functional role and distribution of various Na_V channel subtypes. Despite very low sequence homology with all three scorpion *α*-toxin groups (e.q. Lqh3, Lqh*α*IT and Aah2), the three-dimensional structure of *δ*-HXTX-Mg1a reveals an apparently similar functional surface with a number of these site-3 toxins and spider *δ*-toxins. Several positively charged and aromatic residues of *δ*-HXTX-Mg1a are arranged in a topologically similar manner to those of site-3 toxins. Thus, the structure of *δ*-HXTX-Mg1a provides an important lead for understanding phyla- and subtype-specificity and awaits the determination of the pharmacophore of the toxin.

Acknowledgments–We thank the Suntory Institute for Bioorganic Research, Japan, for continued interest and support. We also thank A.L. Goldin (University of California, Irvine, USA) for sharing $rNa_V1.1$, $rNa_V1.2$, $rNa_V1.3$ and $mNa_V1.6$, G. Mandel (Stony Brook University, Stony Brook, USA) for $rNa_V1.4$, A. George Jr, (Vanderbilt University, Nashville, USA) for $hNa_V1.5$, P. Dietrich (Roche, Palo Alto, USA) for $rNa_V1.7$ and $hNa_V1.8$, L. Isom (University of Michigan, Ann Arbor, USA) and S.H. Heinemann (Friedrich-Schiller-Universität, Jena, Germany) for rβ1, S.C. Cannon (University of Texas, Dallas, USA) for hβ1 and M.S. Williamson (IACR-Rothamsted, Harpenden, UK) for $DmNa_V1$ and tipE. This work was supported in part by grants from the Dirección General de Asuntos del Personal Académico (DGAPA-UNAM) IN220809-3 and CONACyT 49773/24968 to GC, an Australian Research Council Discovery grant DP0559396 to GMN, an Australian Postgraduate Award to MJL, and grants G.0330.06 (F.W.O. Vlaanderen), OT-05-64 (K.U. Leuven) and UA p6/31 (Interuniversity Attraction Poles Program– Belgian State–Belgian Science Policy) to BB and JT.

REFERENCES

1. Catterall, W. A. (2000) *Neuron* **26**(1), 13-25
2. Waxman, S. G., Cummins, T. R., Black, J. A., and Dib-Hajj, S. (2002) *Novartis Found Symp* **241**, 34-51; discussion 51-60
3. King, G. F., Escoubas, P., and Nicholson, G. M. (2008) *Channels* **2**(2), 100-116
4. Catterall, W. A. (1992) *Physiol Rev* **72**(4 Suppl), S15-48
5. Gordon, D. (1997) *Invert Neurosci* **3**(2-3), 103-116
6. Cestèle, S., and Catterall, W. A. (2000) *Biochimie* **82**(9-10), 883-892
7. King, G. F., Gentz, M. C., Escoubas, P., and Nicholson, G. M. (2008) *Toxicon* **52**(2), 264-276
8. Nicholson, G. M., Little, M., and Birinyi-Strachan, L. C. (2004) *Toxicon* **43**(5), 587-599
9. Gordon, D., Karbat, I., Ilan, N., Cohen, L., Kahn, R., Gilles, N., Dong, K., Stühmer, W., Tytgat, J., and Gurevitz, M. (2007) *Toxicon* **49**(4), 452-472
10. Corzo, G., Gilles, N., Satake, H., Villegas, E., Dai, L., Nakajima, T., and Haupt, J. (2003) *FEBS Lett.* **547**(1-3), 43-50
11. Gilles, N., Harrison, G., Karbat, I., Gurevitz, M., Nicholson, G. M., and Gordon, D. (2002) *Eur J Biochem* **269**(5), 1500-1510
12. Little, M. J., Wilson, H., Zappia, C., Cestèle, S., Tyler, M. I., Martin-Eauclaire, M. F., Gordon, D., and Nicholson, G. M. (1998) *FEBS Lett* **439**(3), 246-252

13. Little, M. J., Zappia, C., Gilles, N., Connor, M., Tyler, M. I., Martin-Eauclaire, M. F., Gordon, D., and Nicholson, G. M. (1998) *J Biol Chem* **273**(42), 27076-27083
14. Fletcher, J. I., Chapman, B. E., Mackay, J. P., Howden, M. E., and King, G. F. (1997) *Structure* **5**(11), 1525-1535
15. Pallaghy, P. K., Alewood, D., Alewood, P. F., and Norton, R. S. (1997) *FEBS Lett* **419**(2-3), 191-196
16. Pallaghy, P., Neilsen, K., Craik, D., and Norton, R. (1994) *Protein Sci* **3**, 1833-1839
17. Alessandri-Haber, N., Lecoq, A., Gasparini, S., Grangier-Macmath, G., Jacquet, G., Harvey, A. L., de Medeiros, C., Rowan, E. G., Gola, M., Ménez, A., and Crest, M. (1999) *J. Biol. Chem.* **274**(50), 35653-35661.
18. Böhm, G., Muhr, R., and Jaenicke, R. (1992) *Protein Eng* **5**(3), 191-195
19. Krimm, I., Gilles, N., Sautière, P., Stankiewicz, M., Pelhate, M., Gordon, D., and Lancelin, J. M. (1999) *J Mol Biol* **285**(4), 1749-1763
20. Birinyi-Strachan, L. C., Davies, M. J., Lewis, R. J., and Nicholson, G. M. (2005) *Neuropharmacology* **49**(5), 669-686
21. Gunning, S. J., Maggio, F., Windley, M. J., Valenzuela, S. M., King, G. F., and Nicholson, G. M. (2008) *FEBS J* **275**, 4045-4059
22. Liman, E. R., Tytgat, J., and Hess, P. (1992) *Neuron* **9**(5), 861-871
23. Hamill, O. P., Marty, A., Neher, E., Sakmann, B., and Sigworth, F. J. (1981) *Pflügers Arch* **391**(2), 85-100
24. Rash, L. D., Birinyi-Strachan, L. C., Nicholson, G. M., and Hodgson, W. C. (2000) *Br J Pharmacol* **130**(8), 1817-1824
25. Nicholson, G. M., Blanche, T., Mansfield, K., and Tran, Y. (2002) *Eur J Pharmacol* **452**(1), 35-48
26. Roy, M. L., and Narahashi, T. (1992) *J Neurosci* **12**(6), 2104-2111
27. Wüthrich, K. (1986) *NMR of Proteins and Nucleic Acids*, John Wiley & Sons, New York
28. Schwieters, C. D., Kuszewski, J. J., Tjandra, N., and Clore, G. M. (2003) *J Magn Reson* **160**(1), 65-73
29. Laskowski, R. A., Rullmannn, J. A., MacArthur, M. W., Kaptein, R., and Thornton, J. M. (1996) *J Biomol NMR* **8**(4), 477-486
30. Cierpicki, T., Bania, J., and Otlewski, J. (2000) *Protein Sci* **9**(5), 976-984
31. Pardi, A., Wagner, G., and Wuthrich, K. (1983) *Eur J Biochem* **137**(3), 445-454
32. van Gunsteren, W. F., Billeter, S. R., Eising, A. A., Hünenberger, P. H., Krüger, P., Mark, A. E., Scott, W. R. P., and Tironi, I. G. (1996) *Biomolecular Simulation: The GROMOS96 Manual and User Guide*, Vdf Hochschulverlag AG an der ETH Zürich, Zürich
33. Guex, N., and Peitsch, M. C. (1997) *Electrophoresis* **18**(15), 2714-2723
34. Wilmot, C. M., and Thornton, J. M. (1990) *Protein Eng* **3**(6), 479-493
35. Hutchinson, E. G., and Thornton, J. M. (1994) *Protein Sci* **3**(12), 2207-2216
36. Gunning, S. J., Chong, Y., Khalife, A. A., Hains, P., Broady, K. W., and Nicholson, G. M. (2003) *FEBS*

Lett **554**(1-2), 211-218

37. Nicholson, G. M., Walsh, R., Little, M. J., and Tyler, M. I. (1998) *Pflügers Arch* **436**(1), 117-126
38. Nicholson, G. M., Willow, M., Howden, M. E., and Narahashi, T. (1994) *Pflügers Arch* **428**(3-4), 400-409
39. Black, J. A., Dib-Hajj, S. D., McNabola, K., Jeste, S., Rizzo, M. A., Kocsis, J. D., and Waxman, S. G. (1996) *Mol Brain Res* **43**(1-2), 117-131
40. Ostman, J. A., Nassar, M. A., Wood, J. N., and Baker, M. D. (2008) *J Physiol (Lond)* **586**(4), 1077-1087
41. Fernández, J., Fox, A. P., and Krasne, S. (1984) *J Physiol (Lond)* **356**, 565-585
42. Grolleau, F., Stankiewicz, M., Birinyi-Strachan, L., Wang, X., Nicholson, G. M., Pelhate, M., and Lapied, B. (2001) *J Exp Biol* **204**(Pt 4), 711-721
43. Grolleau, F., and Lapied, B. (2000) *J Exp Biol* **203**, 1633-1648
44. Gilles, N., Krimm, I., Bouet, F., Froy, O., Gurevitz, M., Lancelin, J. M., and Gordon, D. (2000) *J Neurochem* **75**(4), 1735-1745
45. Strichartz, G., and Wang, G. (1986) *J Gen Physiol* **88**, 413-435
46. Schreibmayer, W., Kazerani, H., and Tritthart, H. A. (1987) *Biochim Biophys Acta* **901**(2), 273-282
47. Gordon, D., Merrick, D., Auld, V., Dunn, R. D., Goldin, A. L., Davidson, N., and Catterall, W. A. (1987) *Proc Natl Acad Sci U S A* **84**(23), 8682-8686
48. Gilles, N., Blanchet, C., Shichor, I., Zaninetti, M., Lotan, I., Bertrand, D., and Gordon, D. (1999) *J Neurosci* **19**(20), 8730-8739
49. Leipold, E., Lu, S., Gordon, D., Hansel, A., and Heinemann, S. H. (2004) *Mol Pharmacol* **65**(3), 685-691
50. Maertens, C., Cuypers, E., Amininasab, M., Jalali, A., Vatanpour, H., and Tytgat, J. (2006) *Mol Pharmacol* **70**(1), 405-414
51. Karbat, I., Frolow, F., Froy, O., Gilles, N., Cohen, L., Turkov, M., Gordon, D., and Gurevitz, M. (2004) *J Biol Chem* **279**(30), 31679-31686
52. Karbat, I., Kahn, R., Cohen, L., Ilan, N., Gilles, N., Corzo, G., Froy, O., Gur, M., Albrecht, G., Heinemann, S. H., Gordon, D., and Gurevitz, M. (2007) *FEBS J* **274**(8), 1918-1931
53. Bosmans, F., Rash, L., Zhu, S., Diochot, S., Lazdunski, M., Escoubas, P., and Tytgat, J. (2006) *Mol Pharmacol* **69**(2), 419-429
54. Oliveira, J. S., Redaelli, E., Zaharenko, A. J., Cassulini, R. R., Konno, K., Pimenta, D. C., Freitas, J. C., Clare, J. J., and Wanke, E. (2004) *J Biol Chem* **279**(32), 33323-33335
55. Sheumack, D., Claassens, R., Whiteley, N., and Howden, M. (1985) *FEBS Lett* **181**, 154-156
56. Szeto, T. H., Birinyi-Strachan, L. C., Smith, R., Connor, M., Christie, M. J., King, G. F., and Nicholson, G. M. (2000) *FEBS Lett* **470**(3), 293-299
57. Koradi, R., Billeter, M., and Wüthrich, K. (1996) *Journal of molecular graphics* **14**(1), 51-55

58. Tugarinov, V., Kustanovich, I., Zilberberg, N., Gurevitz, M., and Anglister, J. (1997) *Biochemistry* **36**, 2414–2424

59. Housset, D., Habersetzer–Rochat, C., Astier, J. P., and Fontecilla–Camps, J. C. (1994) *J Mol Biol* **238**(1), 88–103

FOOTNOTES

The atomic coordinates and structure factors (code 2ROO) have been deposited in the Protein Data Bank, Research Collaboratory for Structural Bioinformatics, Rutgers University, New Brunswick, NJ (http://www.rcsb.org/).

[1] These authors contributed equally to this work.

[2] To whom correspondence should be addressed. Tel.: 61-2-9514-2230; Fax: 61-2-9514-8206; E-mail: Graham.Nicholson@uts.edu.au

[3] To whom correspondence should be addressed. Tel.: 52-777-329-1600; Fax: 52-777-317-2388; E-mail: corzo@ibt.unam.mx

[4] The abbreviations used are: HXTX, hexatoxin; Acm, acetamidomethyl; 4-AP, 4-aminopyridine; 3,4-DAP, 3,4-di-aminopyridine; Boc, *tert*. butoxycarbonyl; BrZ, 2-bromobenzyloxycarbonyl; Bzl, benzyl; Xan, xanthenyl; CD, circular dichroism; CZE, capillary zone electrophoresis; DIEA, *N*,*N*-diisopropylethylamine; DRG, dorsal root ganglia; DUM, dorsal unpaired medial; DQF-COSY, double-quantum-filtered correlation spectroscopy; DTT, dithiothreitol; ESI/Q-TOF MS, electrospray ionization / quadrupole time-of-flight mass spectrometry; Gdn·HCl, guanidium hydrochloride; GSH, glutathione; GSSG glutathiol; HBTU, 2-{1H-benzotriazole-1-yl}-1,1,3,3-tetramethyluronium hexafluorophosphate; HEPES-acid, *N*-2-{hydroxyethyl}piperazine-*N*'-{2-ethanesulfonic acid}; HOBt, *N*-hydroxybenzotriazole; ICK, inhibitory cystine knot; K_V channel, voltage-gated K^+ channel; MeBzl, methylbenzyl; MSTX, missulenatoxin; Na_V channel, voltage-gated Na^+ channel; NOE, nuclear Overhauser effect; NOESY, NOE spectroscopy; RMP, resting membrane potential; RP-HPLC, reversed-phase high pressure liquid chromatography; TEA, tetraethylammonium; TFA trifluoroacetic acid; TFE, trifluoroethanol; TOCSY, total correlation spectroscopy; TSP, 3-(trimethylsilyl)[2,2,3,3-$^2H_4$] propionate; TTX, tetrodotoxin.

FIGURE LEGENDS

FIGURE 1. **Primary and secondary structure of *δ*-HXTX-Mg1a.** *A*, Comparison of the primary sequence of *δ*-HXTX-Mg1a and *δ*-HXTX-Mg1b (formerly Magi 14) with currently known members of the *δ*-HXTX-1 family and *δ*-AOTX-Mb1a (*δ*-actinopoditoxin-Mb1a, formerly *δ*-missulenatoxin-Mb1a). Homologies are shown relative to *δ*-HXTX-Mg1a; identities are boxed in *gray* while conservative substitutions are in *gray* italic text. Gaps (dashes) have been inserted to maximize alignment. The disulfide bonding pattern for the strictly conserved cysteine residues determined for *δ*-HXTX-Mg1a (this study), *δ*-HXTX-Ar1a (55) and *δ*-HXTX-Hv1a (15) is indicated above the sequences; it is assumed that *δ*-AOTX-Mb1a (36), *δ*-HXTX-Hs20.1a (8), and *δ*-HXTX-Hv1b (56) have the same disulfide bonding pattern. The percentage identity and homology with *δ*-HXTX-Mg1a is shown to the right of the sequences. *B*, Summary of *δ*-HXTX-Mg1a NMR data. Sequential NOEs, classified as very weak, weak, medium and strong, are represented by the thickness of bars. Filled diamonds indicate backbone amide protons that form hydrogen bonds. $^3J_{NHC\alpha}$ coupling constants are indicated by ↑ (> 8 Hz) and ↓ (< 5.5 Hz). Secondary structure is shown at the bottom of the figure where rectangles represent *β*-turns (the type of turn is

indicated in the rectangle) and arrows represent β-sheets.

FIGURE 2. **Solution structure of δ-HXTX-Mg1a**. *A*, Stereo view of the 20 lowest energy structures of δ-HXTX-Mg1a superimposed over the backbone atoms for the central core (Gly^{2}-Ala^{23} and Gln^{28}-Glu^{32}). *B*, Stereo ribbon representation of the backbone of δ-HXTX-Mg1a showing the location of β-sheets (cyan arrows) and disulfide bonds (red tubes). *C*, Backbone overlay of δ-HXTX-Mg1a (green), δ-HXTX-Hv1a (blue, PDB code 1VTX) and δ-HXTX-Ar1a (cyan, 1QDP). The N- and C-termini are labeled. *D*, Stereo view of the inhibitory cystine knot (ICK) motif of δ-HXTX-Mg1a. The Cys^{14}-Cys^{31} disulfide pierces a loop formed by the Cys^{1}-Cys^{15} and Cys^{8}-Cys^{20} disulfides (red) and the intervening sections of the polypeptide backbone (green) to create a pseudo-knot. Toxin models were prepared using the program MOLMOL (57).

FIGURE 3. **Differential effects of δ-HXTX-Mg1a on TTX-sensitive and TTX-resistant I_{Na} in rat DRG neurons**. *A-B*, Superimposed current traces showing typical effects of a 5 min perfusion with δ-HXTX-Mg1a on TTX-sensitive (*A*) and TTX-resistant (*B*) I_{Na} elicited by a 50-ms test pulse from –90 mV to –10 mV every 10 s. TTX-resistant I_{Na} were recorded in the presence of 200 nM TTX. *C*, Effects of 300 nM δ-HXTX-Mg1a on normalized TTX-sensitive g_{Na}/V relationships (n = 3–5). *D*, Lack of effect of 1 μM δ-HXTX-Mg1a on normalized TTX-resistant g_{Na}/V relationships. In both *C* and *D*, curves were fitted using Eq. 1 in the Materials and methods. *E*, Concentration-response curve of the amplitude of the late TTX-sensitive I_{Na} remaining at 50 ms as a fraction of peak control I_{Na} amplitude (n = 3–7). *F*, Timecourse of slowing of TTX-sensitive I_{Na} inactivation by δ-HXTX-Mg1a. Data shows the I_{Na} remaining at the end of the 50 ms test pulse as a fraction of peak I_{Na} amplitude during perfusion with 300 nM δ-HXTX-Mg1a (open circles), washout with toxin-free external solution (closed circles), and 200 nM TTX (grey circles). The τ_{on} and τ_{off} values for δ-HXTX-Mg1a were determined by fitting single exponential equations to the data points.

FIGURE 4. **Differential effects of δ-HXTX-Mg1a on mammalian Na_V channels expressed in *Xenopus* oocytes**. *A*, Left-hand panels show superimposed current traces illustrating typical effects on mammalian $Na_V1.1$–$Na_V1.3/\beta_1$ and $Na_V1.6$–$1.7/\beta_1$ following a 5 min perfusion with 5 μM δ-HXTX-Mg1a. Currents were elicited every 5 s by 100 ms test pulses from –90 mV to the voltage of maximum activation of the Na_V channel subtype under control conditions. Corresponding right-hand panels show normalized g_{Na}/V (squares) and h_∞/V (circles) relationships in the presence (open symbols), and absence (closed symbols), of 5 μM δ-HXTX-Mg1a (n = 3–6). The g_{Na}/V curves were fitted using Eq. 1 in the Materials and methods while h_∞/V curves were fitted according to Eq. 4. *B*, Superimposed current traces showing typical lack of effect on mammalian $Na_V1.4/\beta_1$, $Na_V1.5/\beta_1$ or $Na_V1.8/\beta_1$ channel currents following a 5 min perfusion with 5 μM δ-HXTX-Mg1a.

FIGURE 5. **Typical effects of δ-HXTX-Mg1a on insect Na_V channels**. Superimposed current traces showing typical effects of (*A*) 15 nM and (*C*) 1 μM δ-HXTX-Mg1a on $DmNa_V1$/TipE channel currents, expressed in *Xenopus* oocytes, and (*E*) 30 nM δ-HXTX-Mg1a on cockroach DUM neuron I_{Na}. Currents were elicited by 50 ms test pulses from –90 mV to –10 mV every 5 s (*A* and *C*) and 10 s (*E*). In panel *E* the amplitude of peak and late I_{Na} increased steadily during initial perfusion with toxin (70 s) before subsequently decreasing to a plateau (5 mins). *B, D* and *F*, Effects of δ-HXTX-Mg1a on normalized g_{Na}/V relationships (squares) and h_∞/V (circles) in expressed $DmNa_V1$/TipE channels (*B* and *D*) and cockroach DUM neurons (*F*). Data shows effects in the presence (open symbols), and absence (closed symbols), of (*B*) 15 nM (n = 7), (D) 1 μM (n = 3) and (*E*) 30 nM δ-HXTX-Mg1a (n = 3–4). The g_{Na}/V curves were fitted using Eq. 1 in the Materials and methods while h_∞/V curves were fitted according to Eq. 4. *G*, Decrease in cockroach DUM neuron I_{Na} amplitude in the presence of 30 nM δ-HXTX-Mg1a following 2 minutes in the absence of stimulation. Currents were subsequently elicited every 10 s. *H*, Concentration-response relationship of the amplitude of I_{Na} remaining at 30 ms ($DmNa_V1$/TipE, closed squares, n = 5) or 50 ms (DUM neurons, grey circles, n = 3–10) as a fraction of peak control I_{Na} amplitude. Data were fitted with a Logistic function.

FIGURE 6. **Typical effects of δ-HXTX-Mg1a on DUM neuron Na_V channel gating**. *A*, Effects of 30 nM δ-HXTX-Mg1a on Na_V channel repriming kinetics in cockroach DUM neurons. Na_V channel repriming rate was determined by normalizing peak I_{Na} elicited during a 50-ms test pulse from –90 mV to –10 mV against peak I_{Na} recorded during a 50-ms conditioning pulse from –90 mV to –10 mV and plotted as a function of the interpulse interval. With interpulse intervals greater than 2 ms, 30 nM δ-HXTX-Mg1a (open circles, $n = 6$) slowed the rate of recovery from inactivation in comparison to controls (closed circles, $n = 6$). *B*, Use-dependent actions of δ-HXTX-Mg1a on Na_V channels in cockroach DUM neurons. Effects of 30 nM δ-HXTX-Mg1a on use dependent decline in I_{Na} during 20 depolarizing test pulses from –90 mV to –10 mV at 30 Hz. Currents were normalized to the peak I_{Na} amplitude of the first pulse in the train in the absence (filled symbols, $n = 6$), and presence (open symbols, $n = 4$), of 30 nM δ-HXTX-Mg1a. *C*, Effects of δ-HXTX-Mg1a (30 nM) at different hyperpolarized holding potentials. Late current (I_{50ms}) amplitude only increased at holding potentials more negative than –140 mV, resulting in a modest but significant increase in the normalized late current (I_{50ms}/I_{pk}) ($n = 3$, *$P < 0.05$, one-way repeated measures ANOVA). *D*, Effects of depolarizing post-pulses on dissociation of 30 nM δ-HXTX-Mg1a were assessed using 10 ms post-pulses to +140 or +200 mV applied immediately following a test pulse to –10 mV from –90 mV every 2 s ($n = 5$). NS, not significant at $P < 0.05$.

FIGURE 7. **Effect of δ-HXTX-Mg1a on action potential duration and firing frequency in cockroach DUM neurons**. *A-B*, Typical superimposed action potentials generated by a single supramaximal current pulse every 10 s before (black traces), and following (grey traces), a 5-min perfusion with 100 nM δ-HXTX-Mg1a. Traces were recorded from a resting membrane potential of –60 mV (*A*), and –90 mV (*B*), following manual hyperpolarization. *C*, Same as panel *B* except stimuli were delivered every minute rather than at 10 s intervals. *D*, Representative effects of a 5-min perfusion with 500 μM 3,4-di-aminopyridine (3,4-DAP, dark grey), 100 nM δ-HXTX-Mg1a (grey), and 100 nM δ-HXTX-Mg1a in the presence of 500 μM 3,4-DAP (light grey), on action potential duration at a resting membrane potential of –60 mV recorded every 10 s. *E*, Same as panel *D* except data was recorded at –90 mV following manual hyperpolarization. Note the slower time scale. *F-H*, Alterations in spontaneous action potential firing frequency and duration. Typical effects on tonic action potential firing before (*F*), and following a 5-min perfusion with 100 nM δ-HXTX-Mg1a recorded at a resting membrane potential of –60 mV (*G*), and a holding potential of –80 mV following manual hyperpolarization (*H*).

FIGURE 8. **Comparison of δ-HXTX-Mg1a structure with other site-3 neurotoxins**. The backbone of toxins, which is shown in ribbon representation is superimposed on the molecular surface. Critical residues are space-filled and colored according to their chemical nature (aromatic, yellow; aliphatic, green; polar, magenta; positively charged, blue and negatively charged, orange). (A) δ-HXTX-Mg1a, (B) δ-HXTX-Hv1a, PDB accession code, 1VTX (14); (C) δ-HXTX-Ar1a, 1QDP (15); (D) Lqh3, 1FH3 (19); (E) Lqhα1T, 1LQH (58); (F) Aah2, 1PTX (59). Structural figures are generated using the PYMOL program (Delano, W.L. The PyMOL Molecular Graphics System (2002) Delano Scientific, San Carlos, CA; www.pymol.org).

SUPPLEMENTAL FIGURE 1S. **Confirmation of the structure and activity of synthetic δ-HXTX-Mg1a**. *A*, Co-elution of synthetic and native δ-HXTX-Mg1a by RP-HPLC. *B*, Overlapping circular dichroism profile of native (open squares) and synthetic (closed circles) δ-HXTX-Mg1a. *C*, Comparable displacement of ^{125}I-Lqhα1T binding to rat brain synaptosomes by unlabelled Lqhα1T (closed triangles), native δ-HXTX-Mg1a (open triangles) and synthetic δ-HXTX-Mg1a (open squares).

SUPPLEMENTAL FIGURE 2S. **Amide proton temperature coefficients in δ-HXTX-Mg1a**. Open squares refer to the values of the temperature coefficients while closed squares represent amide protons regarded as hydrogen-bond donors. The continuous line corresponds to the value of –4.6 ppb/K.

TABLES

Table 1. Structural statistics for the 20 lowest energy structures

Distance restraints	
Intraresidue (| i-j | = 0)	207
Sequential (| i-j | = 1)	181
Medium-range ($2 \leq$ | i-j | ≤ 4)	60
Long-range (| i-j | > 4)	128
Total	576
Ramachandran analysis (residues 2-23, 28-32)[a]	
Residues in most favoured regions (%)	70
Residues in additional allowed regions (%)	25.1
Residues in generously allowed regions (%)	4.2
Residues in disallowed regions (%)	0.7
Atomic r.m.s. differences between 20 conformers (Å)	
Backbone atoms (residues 2-23, 28-32)[b]	0.483 ± 0.005
All heavy atoms (residues 2-23, 28-32)[b]	1.178 ± 0.005
Deviations from idealized covalent geometry	
Bonds (Å)	0.0041 ± 0.00002
Angles (deg.)	0.504 ± 0.002
Impropers (deg.)	0.365 ± 0.002
Mean Xplor energies (kcal/mol)	
E_{total}	-50.30 ± 2.960

[a] PROCHECK-NMR was used to calculate these values.

[b] None of these structures exhibited distance violations $\geq$ 0.4 Å and angle violations $\geq$ 5.0º. r.m.s. differences are given as the mean ± S.E.M

Figure 1

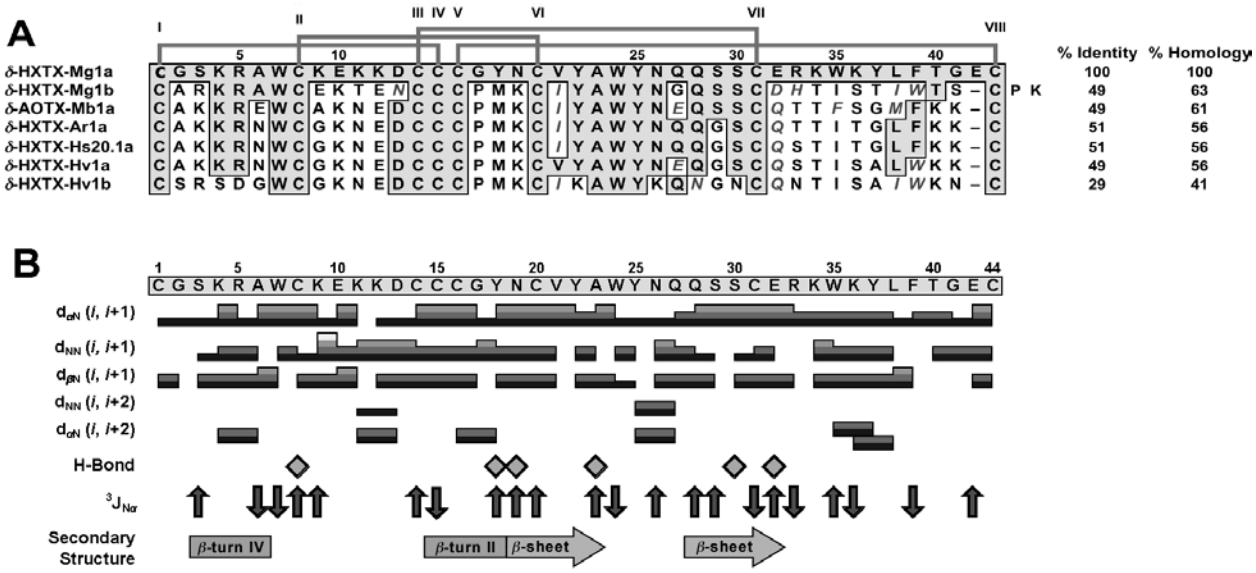
A
I
II
III IV V
VI
VII
VIII
δ-HXTX-Mg1a C G S K R A W C K E K K D C C C G Y N C V Y A W Y N Q Q S S C E R K W K Y L F T G E C
δ-HXTX-Mg1b C A R K R A W C E K T E N C C C P M K C I Y A W Y N G Q S S C D H T I S T I W T S – C P K
δ-AOTX-Mb1a C A K K R E W C A K N E D C C C P M K C I Y A W Y N E Q S S C Q T T F S G M F K K – C
δ-HXTX-Ar1a C A K K R N W C G K N E D C C C P M K C I Y A W Y N Q Q G S C Q T T I T G L F K K – C
δ-HXTX-Hs20.1a C A K K R N W C G K N E D C C C P M K C I Y A W Y N Q Q G S C Q S T I T G L F K K – C
δ-HXTX-Hv1a C A K K R N W C G K N E D C C C P M K C V Y A W Y N E Q G S C Q S T I S A L W K K – C
δ-HXTX-Hv1b C S R S D G W C G K N E D C C C P M K C I K A W Y K Q N G N C Q N T I S A I W K N – C
% Identity % Homology
100 100
49 63
49 61
51 56
51 56
49 56
29 41
B
1 5 10 15 20 25 30 35 40 44
C G S K R A W C K E K K D C C C G Y N C V Y A W Y N Q Q S S C E R K W K Y L F T G E C
$d_{\alpha N}$ (i, i+1)
d_{NN} (i, i+1)
$d_{\beta N}$ (i, i+1)
d_{NN} (i, i+2)
$d_{\alpha N}$ (i, i+2)
H-Bond
$^3J_{N\alpha}$
Secondary Structure
β-turn IV
β-turn II
β-sheet
β-sheet

Figure 2

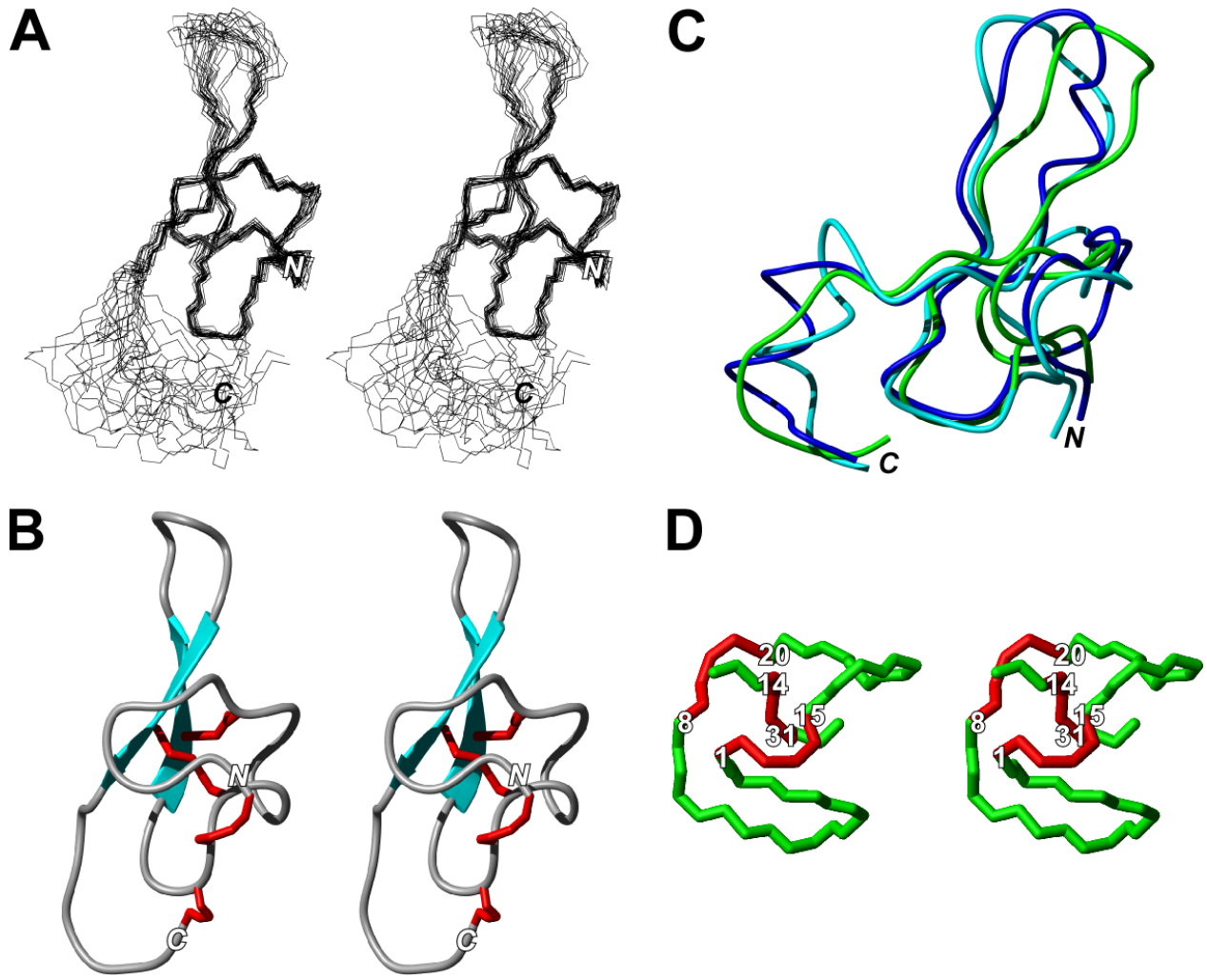

Figure 3

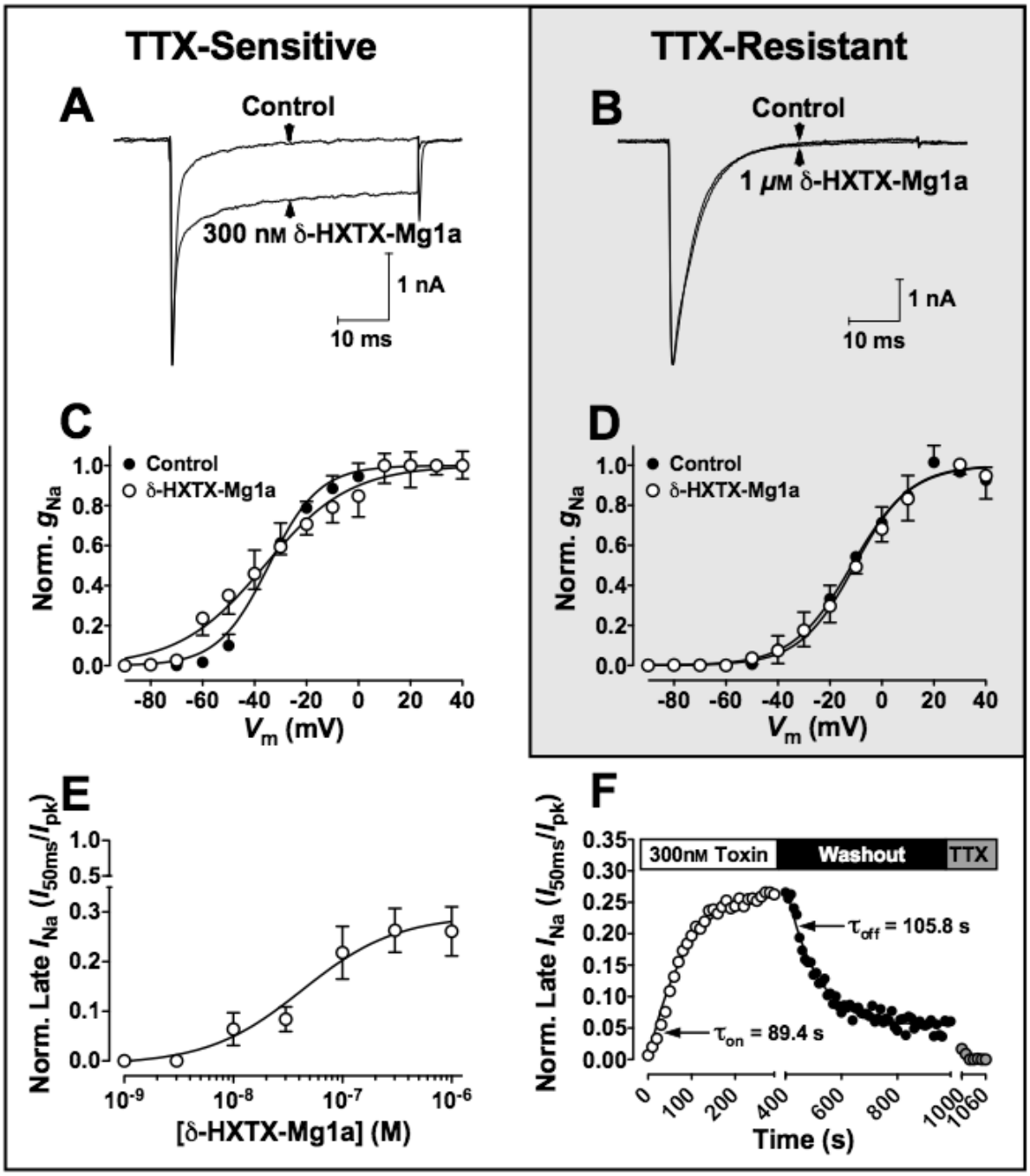
TTX-Sensitive
TTX-Resistant
A
Control
300 nM δ-HXTX-Mg1a
1 nA
10 ms
B
Control
1 μM δ-HXTX-Mg1a
1 nA
10 ms
C
Control
δ-HXTX-Mg1a
Norm. g_{Na}
V_m (mV)
D
Control
δ-HXTX-Mg1a
Norm. g_{Na}
V_m (mV)
E
Norm. Late I_{Na} (I_{50ms}/I_{pk})
[δ-HXTX-Mg1a] (M)
F
Norm. Late I_{Na} (I_{50ms}/I_{pk})
300nM Toxin
Washout
TTX
τ_{off} = 105.8 s
τ_{on} = 89.4 s
Time (s)

Figure 4

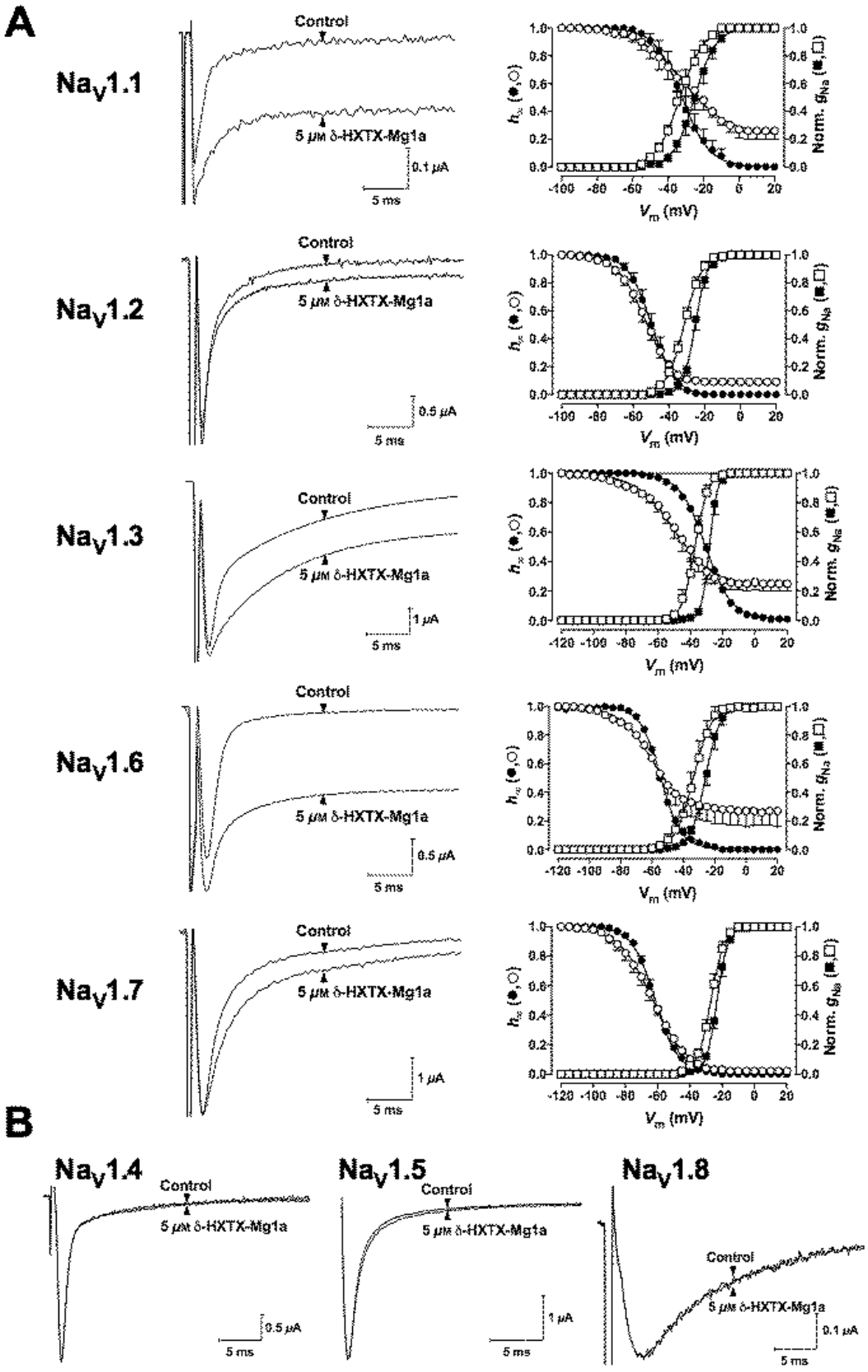
A
Na$_V$1.1
Control
5 μM δ-HXTX-Mg1a
0.1 μA
5 ms
h_∞ (●,○)
Norm. g_{Na} (■,□)
V_m (mV)
Na$_V$1.2
0.5 μA
Na$_V$1.3
1 μA
Na$_V$1.6
Na$_V$1.7
B
Na$_V$1.4
Na$_V$1.5
Na$_V$1.8

Figure 5

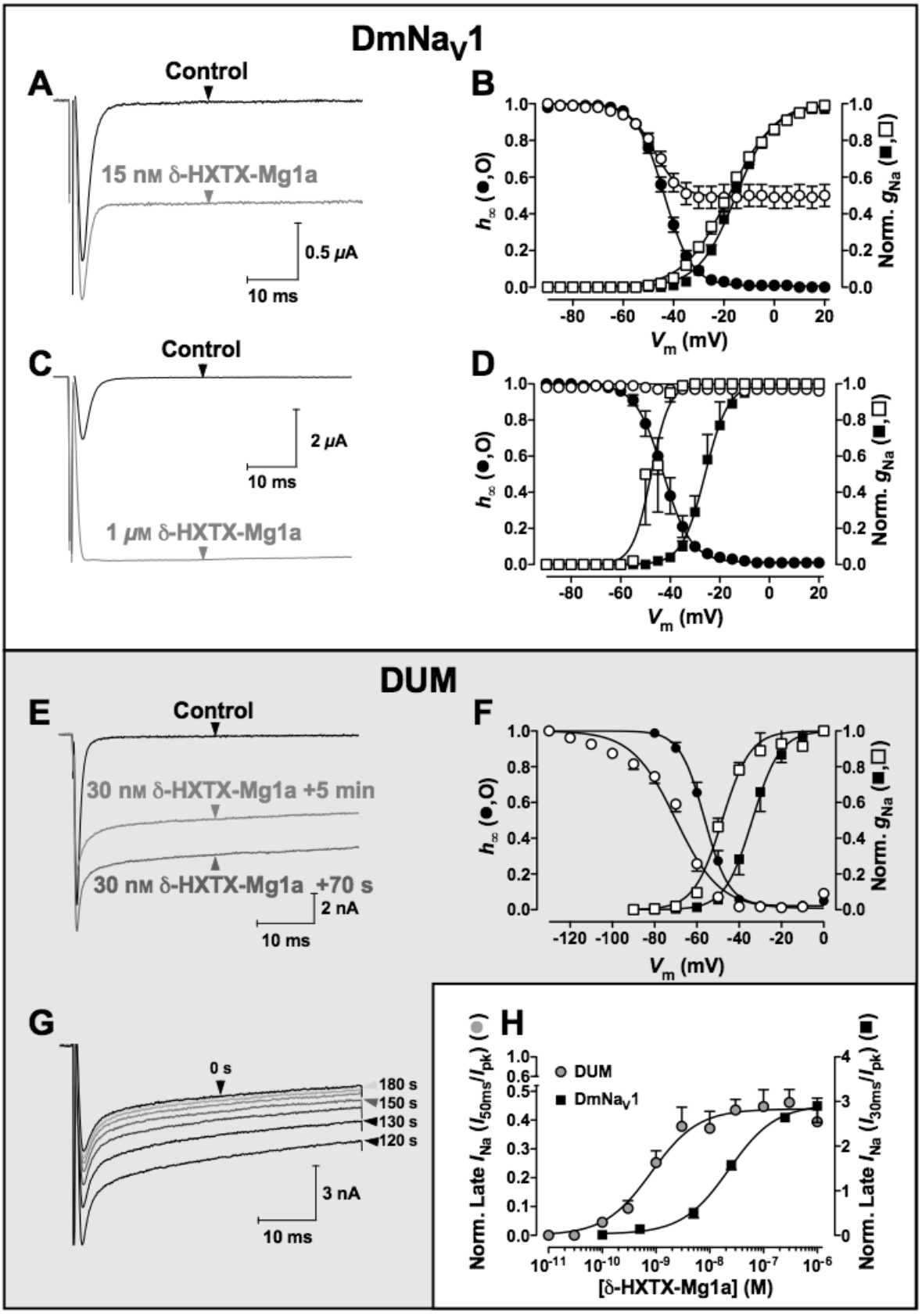
DmNaV1
A
Control
15 nM δ-HXTX-Mg1a
0.5 μA
10 ms
B
h∞ (●,O)
Norm. gNa (■,□)
Vm (mV)
C
Control
2 μA
10 ms
1 μM δ-HXTX-Mg1a
D
h∞ (●,O)
Norm. gNa (■,□)
Vm (mV)
DUM
E
Control
30 nM δ-HXTX-Mg1a +5 min
30 nM δ-HXTX-Mg1a +70 s
2 nA
10 ms
F
h∞ (●,O)
Norm. gNa (■,□)
Vm (mV)
G
0 s
180 s
150 s
130 s
120 s
3 nA
10 ms
H
Norm. Late INa (I50ms/Ipk) (●)
Norm. Late INa (I30ms/Ipk) (■)
DUM
DmNaV1
[δ-HXTX-Mg1a] (M)

Figure 6

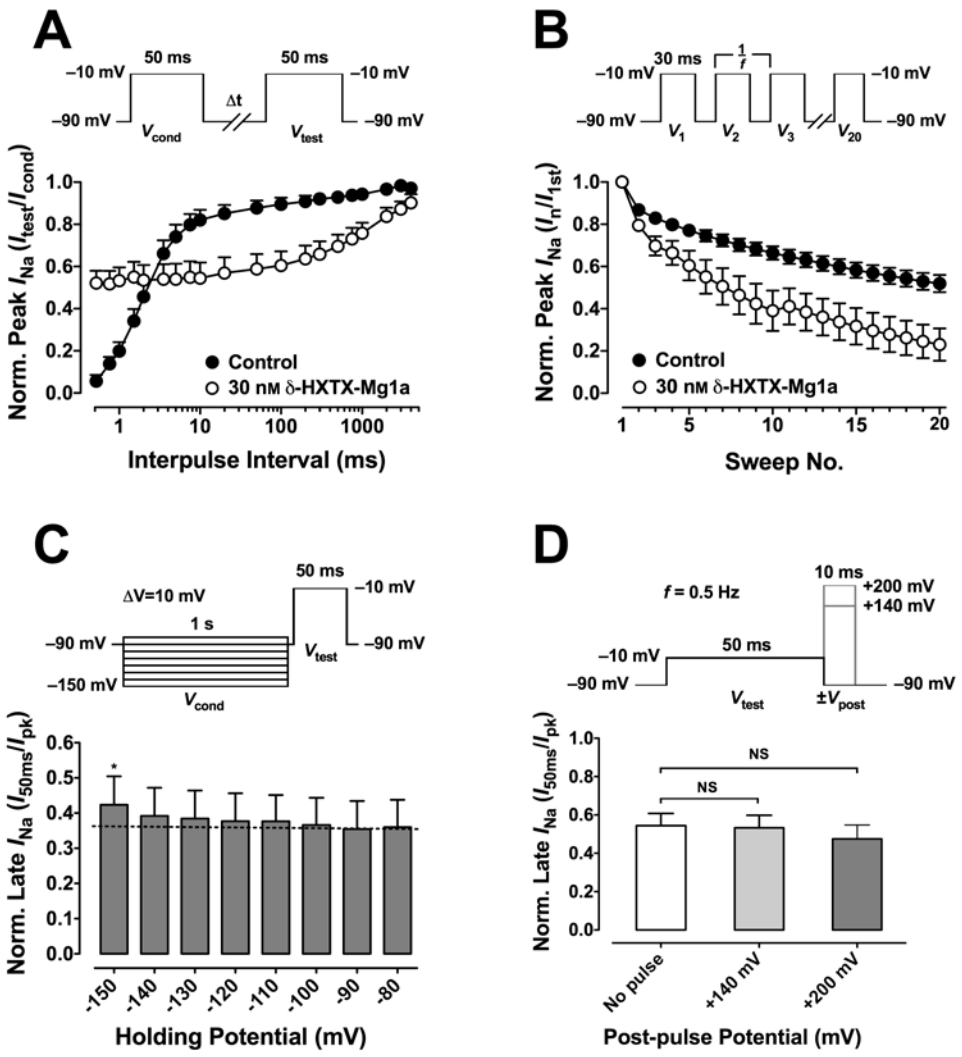
A
50 ms
50 ms
–10 mV
–10 mV
–90 mV
–90 mV
Δt
V_{cond}
V_{test}
Norm. Peak I_{Na} (I_{test}/I_{cond})
Control
30 nM δ-HXTX-Mg1a
Interpulse Interval (ms)
B
30 ms
1/f
–10 mV
–10 mV
–90 mV
–90 mV
V_1
V_2
V_3
V_{20}
Norm. Peak I_{Na} (I_n/I_{1st})
Control
30 nM δ-HXTX-Mg1a
Sweep No.
C
ΔV=10 mV
50 ms
–10 mV
1 s
–90 mV
–90 mV
–150 mV
V_{test}
V_{cond}
Norm. Late I_{Na} (I_{50ms}/I_{pk})
*
-150
-140
-130
-120
-110
-100
-90
-80
Holding Potential (mV)
D
f = 0.5 Hz
10 ms
+200 mV
+140 mV
–10 mV
50 ms
–90 mV
–90 mV
V_{test}
$\pm V_{post}$
Norm. Late I_{Na} (I_{50ms}/I_{pk})
NS
NS
No pulse
+140 mV
+200 mV
Post-pulse Potential (mV)

Figure 7

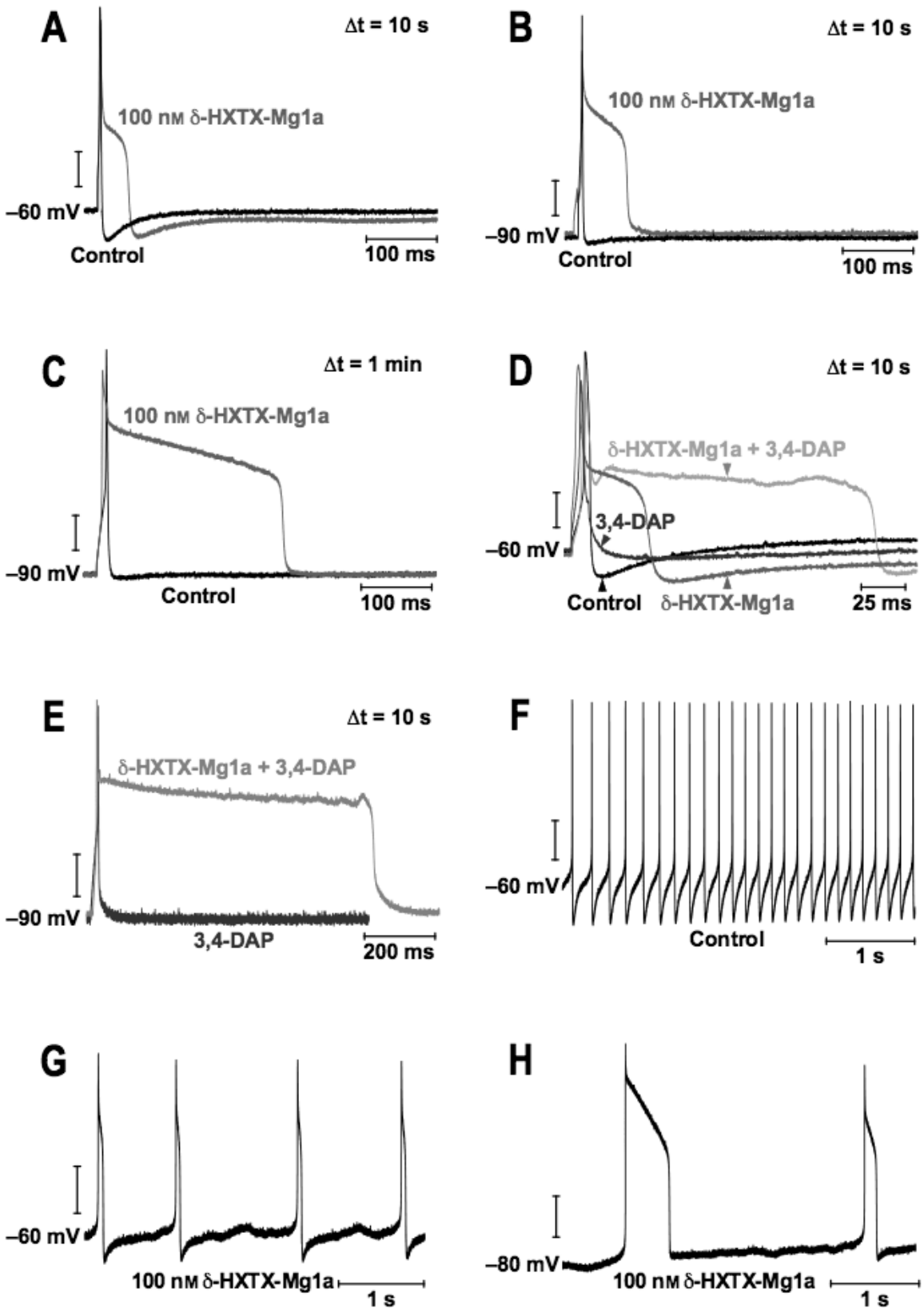
A
Δt = 10 s
100 nM δ-HXTX-Mg1a
–60 mV
Control
100 ms
B
Δt = 10 s
100 nM δ-HXTX-Mg1a
–90 mV
Control
100 ms
C
Δt = 1 min
100 nM δ-HXTX-Mg1a
–90 mV
Control
100 ms
D
Δt = 10 s
δ-HXTX-Mg1a + 3,4-DAP
3,4-DAP
–60 mV
Control
δ-HXTX-Mg1a
25 ms
E
Δt = 10 s
δ-HXTX-Mg1a + 3,4-DAP
–90 mV
3,4-DAP
200 ms
F
–60 mV
Control
1 s
G
–60 mV
100 nM δ-HXTX-Mg1a
1 s
H
–80 mV
100 nM δ-HXTX-Mg1a
1 s

Figure 8

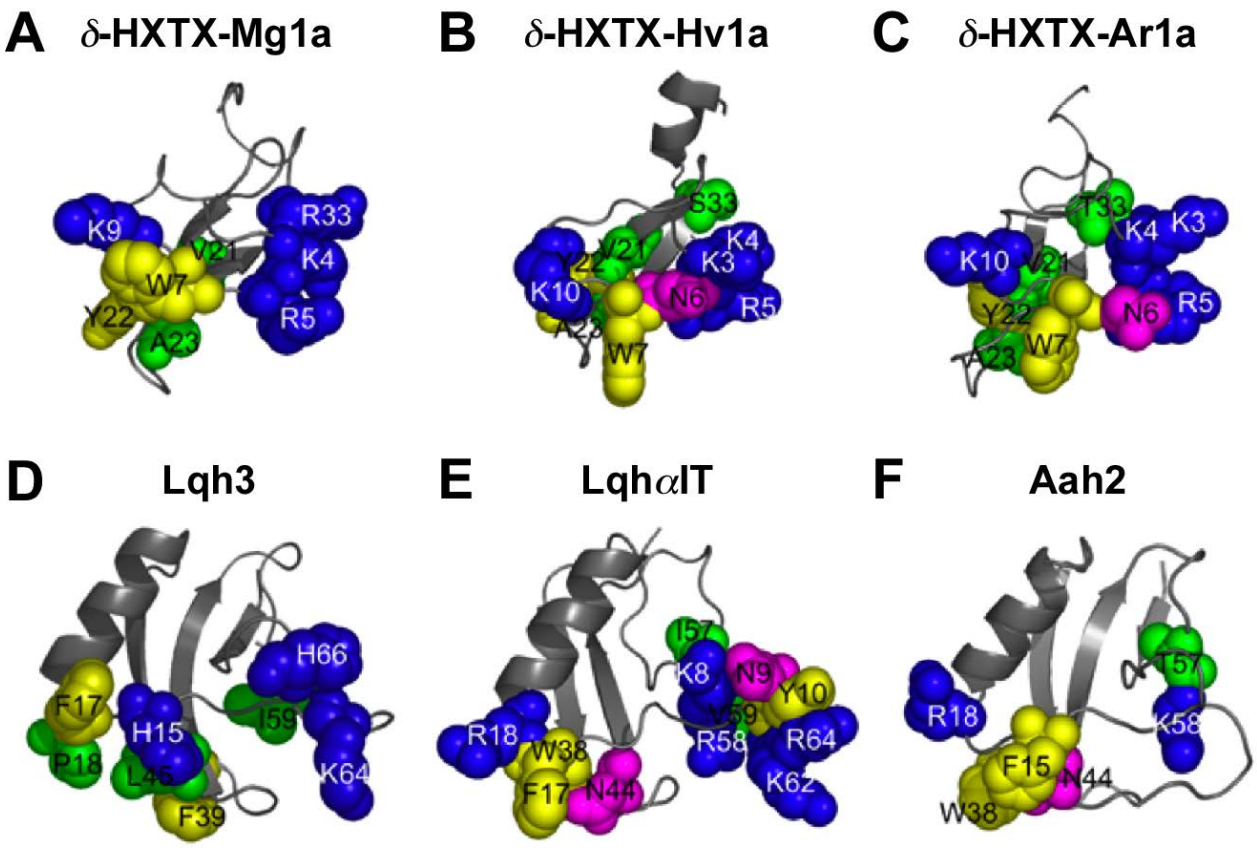
A δ-HXTX-Mg1a
K9
R33
V21
K4
W7
Y22
R5
A23
B δ-HXTX-Hv1a
S33
V21
K4
Y22
K3
K10
N6
R5
W7
C δ-HXTX-Ar1a
T33
K4
K3
K10
V21
Y22
N6
R5
W7
D Lqh3
H66
F17
H15
I59
P18
L45
K64
F39
E LqhαIT
I57
K8
N9
Y10
R18
W38
R58
R64
F17
N44
K62
F Aah2
T57
R18
K58
F15
N44
W38